



HAL
open science

Quantifying uncertainties in signal position in non-resolved object images: application to space object observation

Francois Sanson, Carolin Frueh

► **To cite this version:**

Francois Sanson, Carolin Frueh. Quantifying uncertainties in signal position in non-resolved object images: application to space object observation. *Advances in Space Research*, In press, 10.1016/j.asr.2018.12.040 . hal-01968808v2

HAL Id: hal-01968808

<https://hal.science/hal-01968808v2>

Submitted on 4 Jan 2019 (v2), last revised 14 Jan 2019 (v3)

HAL is a multi-disciplinary open access archive for the deposit and dissemination of scientific research documents, whether they are published or not. The documents may come from teaching and research institutions in France or abroad, or from public or private research centers.

L'archive ouverte pluridisciplinaire **HAL**, est destinée au dépôt et à la diffusion de documents scientifiques de niveau recherche, publiés ou non, émanant des établissements d'enseignement et de recherche français ou étrangers, des laboratoires publics ou privés.

Quantifying uncertainties in signal position in non-resolved object images: application to space object observation

Francois Sanson^{a,*}, Carolin Frueh^b

^a*Inria Bordeaux Sud-Ouest, 200 Rue de la Vieille Tour, 33405 Talence, France*

^b*School of Aeronautics and Astronautics, Purdue University, West Lafayette IN 47906, USA*

Abstract

Charged Coupled Devices (CCDs) and subsequently Complementary metal-oxide-semiconductor (CMOS) detectors revolutionized scientific imaging. On both the CCD and CMOS detector, the generated images are degraded by inevitable noise. In many applications, such as in astronomy or for satellite tracking, only unresolved object images are available. Strategies to estimate the center of the non-resolved image their results are affected by the detector noise. The uncertainty in the center is classically estimated by running prohibitively costly Monte Carlo simulations, but in this paper, we propose analytic uncertainty estimates of the center position. The expressions that depend on the pixel size, the signal to noise ratio and the extension of the object signal relative to the pixel size are validated against rigorous Monte Carlo simulations with very satisfying results. Numerical tests show that our analytic expression is an efficient substitute to the Monte Carlo simulation thereby reducing computational cost.

Keywords: Space Situational Awareness

1. Introduction

Space object observation heavily relies on Charged Coupled Devices (CCDs)

*Corresponding author. Tel.: +33(0)5 24 57 41 12

Email address: francois.sanson@inria.fr (Francois Sanson)

and Complementary Metal–Oxide–Semiconductor (CMOS) detectors. For images of objects that are too far away from the sensor and or too small for the optic setup, only non-resolved images are available. Fig.2 shows a perfectly noiseless non-resolved object image. Physically speaking, the bright dot corresponds to the first maximum of the diffraction pattern, for a round aperture, the so-called Airy disk. The main maximum contains over 80 percent of the whole light received from the object. Higher order maxima are normally not discernible and hence not visible on the final image.

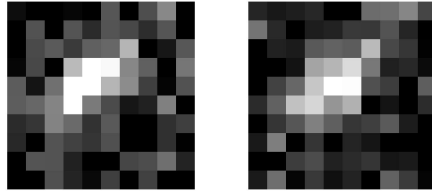
As the sensing process, including the photon reception, the photo-electron release and the read-out process, is taking place on the quantum level, it is by nature a stochastic process. This means that the image generated by a sensor differs across repeated experiments despite having exactly the same amount of light entering the detector. Classically, the detector response has been modeled as a Poisson process with the expectation value and variance corresponding to the nominal irradiation value entering the detector [1]. An example of four synthetically generated representations of the same irradiation entering the detector are plotted in Fig. 1. Besides the stochastic sensing process of the irradiation received from the object, there are two additional types of noise sources that corrupt the object images and impact object image detection and position estimation. One source is the other external light sources that enter the detector while the second source comes from noise generated by the detector itself. Given that the detector is never at zero Kelvin, thermal motion leads to so-called dark noise, that is even present when the shutter is not opened. Furthermore, there is the noise generated by the read-out process itself and the truncation error, as only integer pixel values can be recorded in ADUs. Further image processing step such as background subtraction introduce additional noise sources. Extensive description of CCD functioning is presented in [2], a good CCD signal noise generation is available in [3].

In many applications using images featuring non-resolved signals, such as detection and tracking of stellar objects or satellites, or tracking of blood cells in microscopic imaging for example in medicine or biology, object detection and

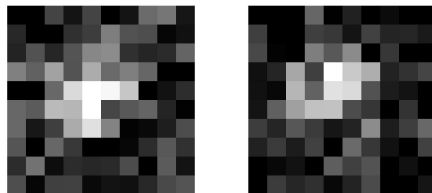
position estimation beyond the pixel size level is challenging [4, 5, 6, 7, 8, 9, 10]. Tracking algorithms rely on the precise estimation of the signal position at the subpixel level. This is usually done via determining the center, often called center, of the object signal. The center is then assumed to be the object position at the mid-exposure time. Because of the image noise and the stochastic nature of the detection, the center location is not straightforward. In practice, there are two main classes of techniques to find the center of a non-resolved digital object image: one is to fit a two-dimensional function over the pixel values of the object images and its surrounding pixels while the second finds the centroid of the object image [6, 1, 3]. In the former case, for slightly distorted object images, a Gaussian function fitting is often performed using a maximum likelihood estimator [11, 12, 13, 14, 15]. However, Gaussian fitting is ill-suited to fit object images, which significantly deviate from the Gaussian shape, respectively the Airy disk. Object shapes can significantly deviate from the Gaussian shape due to camera distortion, however, often times models can be applied to correct for those in the image processing and due to atmospheric turbulence in the case of ground-based observations and very short exposure times. Shape independent centroiding methods include the so-called center of mass or also named centroid methods. They produce reliable results for highly distorted images, for which surface fitting often fails. Both methodologies require that the background of the images has been subtracted. Description of image processing pipelines for astrometric observations of near-Earth objects is discussed in [16, 6, 17, 18].

As with any sensing and estimation problem, the estimated center differs for different representations of the same irradiation reaching the detector. This is illustrated in Fig. 1 and Fig. 3. Fig. 1 shows the same object signal in four different realizations. Fig. 3 shows the bar plot of pixel values, the fitted Gaussian surface and the centers that have been determined for identical irradiation reaching the detector. For the applications, it is of utmost interest to have a representation of the uncertainty associated with the center. The variance in the brightness of a pixel value can be computed using the inverse of the signal to noise ratio [2, 3]. On the other hand, the variance in the center position is

not just a straightforward estimation problem.



(a) Signal realization 1 (b) Signal realization 2



(c) Signal realization 3 (d) Signal realization 4

Figure 1: Four realizations of the same noiseless signal (cf Fig. 2)

As a result, center uncertainties are often determined with costly Monte Carlo methods based on simulated images. This computationally intensive process is sought to be avoided.

The major contribution of this paper is the derivation of an analytical approximation of center position variance that does not require any Monte Carlo simulations. The derived expression is thoroughly compared to alternative expensive methods such as Monte Carlo. The derived expressions are also compared to existing analytical expressions [19, 20, 21]. All the tests show that the estimation of the center variance is a good approximation of the Monte Carlo results even for relatively small and cropped signals. Numerical experiments show that the derived expression is valid for signals as small as 4 pixels per FWHM and an SNR at 5. In this work, it is also shown that the previous estimates of this lower bound systematically underestimate the true variance, based upon the

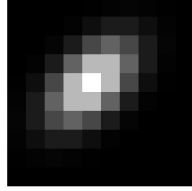
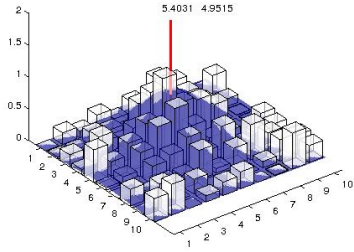


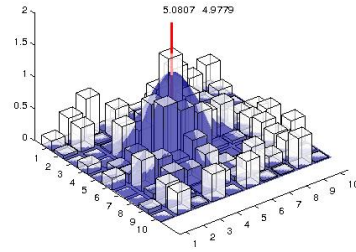
Figure 2: Noiseless signal

comparison with Monte Carlo simulations. For object images, which are spread over less than four pixels, a Bayesian formulation of the problem is introduced. Realistic bounds on the object image center position on the sub-pixel level are provided based on the pixel scale and the signal to noise ratio of the brightest pixel. Finally, a look-up table with reference values is provided. Preliminary work on this topic has been published by the authors in [22].

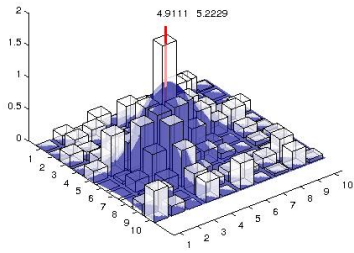
The paper is organized as follows: In the second section, we describe the center estimation process of a noisy non-resolved object image on a pixel grid using a Gaussian fitting. In the third section, the improved estimation of the center position uncertainty is shown and analytical expressions are derived. Based on the derivations, the fourth section provides the validation of the methodology via comparison with Monte Carlo simulations and Bayesian estimation. In the fifth section, application guidelines for the variance computation in observed image frames are provided. The findings are summarized in the conclusions. In Appendix B, a look-up table for fast application in observations can be found.



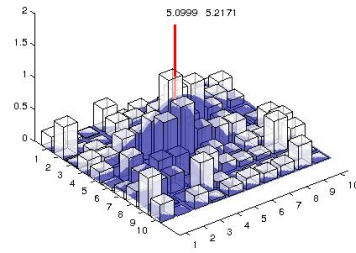
(a) Signal realization 1



(b) Signal realization 2



(c) Signal realization 3



(d) Signal realization 4

Figure 3: Four realizations of the same signal (cf Fig. 2) with fitted Gaussians. The red line indicates the position of the center in each case

2. Overview of Object Image Centroiding in Noisy Images

In this section, the process of finding an object image center in the presence of noise is summarized. First, the expressions for the signal in the pixels containing the object image are derived. Further details on the derivation of the CCD equation and advances in the presence of ambiguous pixels can be found in [23, 22]. Secondly, the process of the maximum likelihood estimation is shown. Details on center determination techniques via Gaussian fitting can be found in [11, 12, 13, 14, 15].

2.1. Signal of the Object Image Pixels

The Gaussian or other parametrized surface is fitted to the signal after background subtraction. The total signal S of all pixels containing the object image can be written as [22]:

$$S = \sum_i^{n_{pix}} S_i + R_i - B_{est} \quad (1)$$

where n_{pix} is the number of pixels containing the object image (i.e. the diffraction Airy disk). The pixels are indexed by i . S_i is the truncated signal distribution of each pixel as defined in [22]. The truncation process is due to the fact that only integers can be reported from the CCD during the electron to ADU conversion. Defining the gain g , one ADU corresponds to g photoelectrons. R_i is the readout noise. B_{est} is the estimated background that is subtracted.

B_{est} is the estimated background defined in [22, 3] as :

$$B_{est} = \frac{1}{n_B} \sum_i^{n_B} S_i + R_i \quad (2)$$

with n_B is the number of pixels used for the background estimation.

Eq. 1 is the sum of random variables that follow different distributions. The following assumptions are made for simplification in order to approximate Eq. 1 as a sum of Gaussian random variables. Assuming that the gain is small or alternatively that the CCD resolution is extremely high (hypothesis 1) the truncated Poisson S_i can be interpreted as a Poisson random variable with a good level of accuracy. For the actual signal on the CCD, it can be assumed that the mean signal intensity is such that $\lambda_{ext,i} + \lambda_{obj,i} + \lambda_{D,i} \gg 1 \quad \forall i$ (hypothesis 2). The use of the Central Limit Theorem can account for modelling both, the signal and the background as normal distributions: $S_i \sim \mathcal{N}(\lambda_{ext,i} + \lambda_{obj,i} + \lambda_{D,i}, \sqrt{\lambda_{ext,i} + \lambda_{obj,i} + \lambda_{D,i}})$ and $B_{est} \sim \mathcal{N}(\lambda_{ext,i} + \lambda_{D,i}, \sqrt{\frac{\lambda_{ext,i} + \lambda_{D,i}}{n_b}})$. In the latter, the number of pixels used in the background determination n_B is assumed to be large (hypothesis 3), which is advantageous for precise background determination, as shown in Eq.2. Note that in order to preserve the

homogeneity of S , we denote $Var(S) = \lambda_{S,i} \times 1_s$, where 1_s only carries the unit of energy. R_i can be taken to be Gaussian as well [3, 2], and is assumed to be constant over the signal pixels (hypothesis 4). Whereas the latter is a good approximation for a CCD, the assumption might be violated for object images spread out over a large number of pixel on a CMOS detector. Finally under the assumption previously stated, the effective signal in the i^{th} pixel S_i as in Eq. 1 is the sum of three independent Gaussian random variables:

$$S_i = \lambda_{S,i} - \lambda_{\text{ext},i} + \lambda_{D,i} + \mathcal{N}\left(0, 1_s \times \sqrt{\lambda_{S,i} + \frac{\lambda_{\text{ext},i} + \lambda_{D,i}}{n_b} + \sigma_R^2}\right), \quad (3)$$

where σ_R^2 is the variance of the readout noise at the i th pixel. Note that the noise model presented only considers noise sources due to the detector (CCD or CMOS). Other uncertainty sources such as the atmosphere turbulence are neglected. Nevertheless, if the noise due to the atmospheric turbulence (or any additional noise) is modeled by an independent Gaussian noise of amplitude σ_{atmo} , the signal distribution is Gaussian and therefore the work presented can be used replacing σ_R^2 with $\sigma_R^2 + \sigma_{atmo}$. Additionally, for extremely faint signals, the Poisson noise may not be well approximated by a Gaussian random variable, in this case, a sum of Gaussian and Poisson noise should be considered. This case is out of the scope of this work and in the following we solely consider pure Gaussian noise. Using a Maximum Likelihood Estimator, a Gaussian curve is fitted to the signal:

$$G = A e^{\left(-\frac{1}{2}(c_1(x_i - x_0)^2 + 2c_3(x_i - x_0)(y_i - y_0) + c_2(y_i - y_0)^2)\right)}. \quad (4)$$

noting $\theta = (A, x_0, y_0, c_1, c_2, c_3)$ where A is the amplitude, x_0 and y_0 the center of the fitted Gaussian on the pixel grid and c_1 , c_2 and c_3 the coefficients of the inverse covariance matrix. The position of the object image on the pixel grid then is denoted by x_0, y_0 . The Gaussian fitting can be done for instance using algorithm from [19]

3. Uncertainty Quantification of the signal center

In this section, we derive analytical uncertainty estimates of the signal center estimation. The Gaussian fitting can only be applied to a specific realization of the stochastic object image generation process according to the distributions of the terms in Eq.2. Under the assumptions discussed in the previous section, the signal distribution is a sum of Gaussian random variables, Eq.3. As discussed in the introduction and illustrated Fig 1 there, different realizations lead to different centers. Fig.3 shows the 3D representation of noise affected images with the fitted Gaussian surface.

We present two common approaches to quantify the uncertainty in the estimation of the parameters : a maximum likelihood estimation as it is carried in [19, 24] or a Bayesian approach [25]. Both methods tackle a problem from a different angle so the uncertainty in the estimation are in general different. The maximum likelihood estimation focuses on estimating the deterministic parameters θ_{true} and then estimates the uncertainty in the estimator $\hat{\theta}$. On the contrary, with the Bayesian approach, one considers the distribution of Θ for a given set of measurements. While in the case of uniform priors, the maximum a posteriori derived from the Bayesian posterior distribution and the ML are equivalent, the uncertainty are only equivalent asymptotically (if the number of pixels is large enough) as a consequence of the Bernstein Von Mises theorem. This difference will be illustrated for small enough signals when comparing the Monte Carlo verification and the Bayesian approach for quantifying uncertainties .

When fitting a Gaussian surface to the signal, one needs to estimate θ , which holds the six Gaussian surface parameters, namely, A, c_1, c_2, c_3 along with the center x_0, y_0 . However, often in imaging, only the center, comprising of two parameters are of major interest. Hence, the first four parameters may be treated as nuisance parameters. The nuisance parameter estimation not only influences the nominal values of the remaining quantities of interest, but also affects the

variance in the parameters of interest. Uncertainty in their estimation leads to increased uncertainty in the parameters of interest. As stated in [26] and [27] the variance with nuisance parameters is always larger than without nuisance parameters.

3.1. Rao-Cramer lower bound

Under regularity assumptions on the likelihood function, for any unbiased estimator, there exists a variance lower bound [28]. In our case, the maximum likelihood (ML) estimator asymptotically reaches this lower bound [28, 27] and therefore this lower bound can be used as an approximation of the center position variance. We define the Fisher information as

$$F(\theta) = \mathbb{E} \left[\frac{\partial^2 l}{\partial^2 \theta_i \theta_j} \right], \quad (5)$$

where \mathbb{E} denotes expected value with respect to the likelihood. As explained in [28], the Fisher information corresponds to the average amount of information available in the sample. The Fisher information as derived in [19] is given in Appendix C. The Rao Cramer lower bound (RCLB) variance is related through the following inequality to the Fisher information:

$$\text{Var}_{s_1 \dots s_n}(\hat{\theta}) \geq F(\theta)^{-1}. \quad (6)$$

Which means that the variance of the Rao Cramer lower bound is always larger or equal to the inverse of the Fisher information. If the number of pixels used in the ML estimation is sufficiently large, the ML estimator converges toward a Gaussian distribution ([24, 27]):

$$\hat{\theta} \sim \mathcal{N}(\theta_{\text{true}}, F(\theta)^{-1}). \quad (7)$$

In that case, the lower bound will be reached, the inequality then becomes an equality and a good analytical estimation of the RCLB variance becomes available.

In many cases, simple analytical expressions of the Fisher information are not

available, but in our case, previous works [20, 19] have managed to derive such expression under the following assumptions:

1. Flat noise: σ is constant over all pixels of the signal.
2. The profile is well sampled: the pixel size is constant and small compared to the object image size. In other words we have $\delta_x, \delta_y \ll \frac{1}{c_1^{0.5}}, \frac{1}{c_2^{0.5}}$ where δ_x and δ_y are the CCD pixel dimensions.
3. The entire profile of the object image is sampled
4. The irradiance at the center of the pixel corresponds to the received irradiance for the same pixel. In other words: $\xi_n = \delta_x n$ and $\eta_m = \delta_y m$.
5. The signal distribution is Gaussian within each pixel

Assumption 5 and 1 are tied together since the noise intensity can only be constant when the noise is Gaussian distributed. Note that assumption 4 is not explicitly stated in [20, 19] and it is only used when deriving an approximation of the RCLB and does not apply to the MLE results. The profile of the object image when approximated with a Gaussian is theoretically infinitely wide spread over the whole pixel grid. The exact expression for the Fisher information as derived in [19] and can be found in Appendix C. The Fisher information terms can be decomposed into sums of the form:

$$\sum_{m,n=0}^{n_{\text{pix}}} R_{n,m} \xi_n^i \eta_m^j \text{ with } j, i \leq 4 \quad (8)$$

where $R_{n,m} = \frac{\delta_x^2 \delta_y^2 E_{n,m}^2}{2\sigma^2}$ and

$E_{n,m} = \exp\left(-\frac{1}{2} (c_1(x_n - x_0)^2 + 2c_3(x_n - x_0)(y_m - y_0) + c_2(y_m - y_0)^2)\right)$, $\xi_n = x_n - x_0$ and $\eta_m = y_m - y_0$.

The task now is to compute the sums. Their derivation can be involved so most of the derivation is left in Appendix E and Appendix D while this paragraph focuses on the assumptions made to carry out the calculations. Under the hypotheses one through four above, [19] the sums can be approximated with their corresponding integrals; this approach was already used in [21]. This approximation is justified by classical results on Riemann integrals and accurate

up to the second order in δ_x, δ_y , the pixel size in x and y directions. However, it is found that the assumptions one through four are not well justified for faint or truncated signals, for instance when the signals overlap or when a sub-frame technique has to be used. Assumption one is significantly violated in general, since as shown in section 2.1, the noise squared is approximately the sum of a Poisson noise that scales as the signal intensity and a readout noise that is constant across the image. In [19] both limiting cases where the noise is constant and when it is purely Poisson are investigated. In this work we only consider the constant noise case that is not valid for large signals or with low readout noise. Hypothesis two is not valid for undersampled object images where the pixel scale is too large. The third assumption used in [19] is often challenging to comply with in practice. Firstly, when there is more than one object image in the whole observation frame, the object image is cropped over a finite number of pixels. Furthermore, the background necessarily changes across the domain and clashes with hypothesis one. In practice, a sub-frame technique with limited size sub-frames is used and hence assumption three is violated. Assumption 4 is in general violated. A priori, the center position has no reason to be in the center of a pixel. This is also confirmed by real observations [18]. In general, we have $\eta_m = u_y + \delta_y m$ and $\xi_n = u_x + \delta_x n$, where u_x and $u_y \in [0, \frac{\delta_x}{2}) \times [0, \frac{\delta_x}{2})$. In order to relax the assumptions to better fit the conditions of actual observations, a truncated signal is assumed not symmetric with the pixel grid, avoiding assumptions three and four, while keeping assumptions one, two and five.

Denoting a and b as the cropping boundaries (ie. the portion of the considered signal lies in the rectangle $[-a; a] \times [-b; b]$), it is further assumed that $a\sqrt{\frac{D}{c_2}} \gg 1$ and $b\sqrt{\frac{D}{c_1}} \gg 1$. Note that $D = c_1 c_2 - c_3^2$. Due to this unsymmetrical distribution of the pixels around the center of the object and the cropping around the center of the object image, the substitution of sums with their integrals is only accurate up to the first order in δ_x, δ_y for some terms of the Fisher information. In order to get improved analytical expressions for Eq. 10, u_x and u_y are un-

known a priori. They are modeled with a uniform distribution $\mathcal{U}[0, \frac{\delta_x}{2}]$ (resp. $\mathcal{U}[0, \frac{\delta_y}{2}]$) [21] and the sums are approximated with its corresponding integral. A change of variable yields the following approximation for $\sum_n \sum_m R_{n,m} \xi_n^i \eta_m^j$ with a second order accuracy in the pixel size $\delta_{x,y}$:

$$\sum_n \sum_m R_{n,m} \xi_n^i \eta_m^j \approx J_{x^i y^j} = \int_{-a+u_x}^{a+u_x} \int_{-b+u_y}^{b+u_y} x^i y^j e^{-(c_1 x^2 + 2c_3 xy + c_2 y^2)} dx dy \quad (9)$$

This approximation is key to derive an analytical expression for the RCLB. The calculations in the rest of this section aim at deriving analytical expressions for $J_{x^i y^j}$. Using Eq. 9, the $J_{x^i y^j}$ are then injected in the analytical expression for the Fisher Information Eq. C.1 from which the RCLB can be derived.

Note: The Fisher information computed in [19] only uses the constant terms in δ (order 0^{th}). Unfortunately, this approximation leads to a covariance matrix where the position parameters (x_0, y_0) and the nuisance parameters appear to be uncorrelated, which we know is untrue. In the appendix it is shown that, in general

$$\sum_{m=0}^{n_{\text{pix}}} R_m \xi_n^i \eta_m^j = \sum_n \sum_m R_{n,m} \xi_n^i \eta_m^j = 0 + \epsilon(u_x, u_y), \text{ if } i+j \text{ is odd,} \quad (10)$$

with $\epsilon \propto \delta_{x,y}$. The sum in Eq. 10 is equal to zero, when the signal/object image is uncropped or u_x and u_y are non zero. Because we do assume a cropped signal, all the terms, where $i+j$ are even and when $i+j$ are odd they are non-zero.

Derivation of analytic expression of $J_{x^i y^j}$ (Eq. 9) , when $i+j$ is odd

We define

$$f_{i,j}(x, y) = x^i y^j e^{-(c_1 x^2 + 2c_3 xy + c_2 y^2)} \quad (11)$$

using the symmetries of $f_{i,j}$, we have $\int_{[0, a-u_x] \times [0, b-u_y]} f_{i,j}(x, y) dx dy = - \int_{[0, -a+u_x] \times [0, -b+u_y]} f_{i,j}(x, y) dx dy$ and

$\int_{[0, -a+u_x] \times [0, b-u_y]} f_{i,j}(x, y) dx dy = - \int_{[0, a-u_x] \times [0, -b+u_y]} f_{i,j}(x, y) dx dy$. The in-

tegral in Eq.9 can hence be decomposed and simplified into:

$$J_{x^i y^j} = \int_{a-u_x}^{a+u_x} \int_{-b}^b f_{i,j}(x,y) dx dy + \int_{-a}^a \int_{b-u_y}^{b+u_y} f_{i,j}(x,y) dx dy. \quad (12)$$

Note: The square of size $[a, a+u_x] \times [b, b+u_y]$ is included and $[a-u_x, a] \times [b-u_y, b]$ is counted twice but they are small (order two in the pixel size). Assuming u_x and u_y are small, Taylor series expansions around a and b leads to the following expression:

$$\begin{aligned} J_{x^i y^j} &= 2u_x a^i \exp\left(-\frac{a^2 D}{c_2}\right) \int_{-b}^b y^j \exp\left(-\frac{y^2 D}{c_1}\right) dy \\ &+ 2u_y b^j \exp\left(-\frac{b^2 D}{c_1}\right) \int_{-a}^a x^i \exp\left(-\frac{x^2 D}{c_2}\right) dx. \end{aligned} \quad (13)$$

Eq. 13 shows that $J_{x^i y^j}$ scales like $u_x a^i \exp\left(-\frac{a^2 D}{c_2}\right)$ that should be small according to our hypotheses. For completeness, full calculations of the integrals are provided in Appendix D, however their exact expressions are not necessary for the remainder of this study as they will constitute negligible components of the Fisher information.

Computation of the $J_{x^i y^j}$ (Eq. 9), when $i + j$ is even

We now focus on the even integrals ie. the integrals for which $i + j$ is even by computing:

$$J_{x^i y^j} = \int_{-a+u_x}^{a+u_x} \int_{-b+u_y}^{b+u_y} x^i y^j e^{-(c_1 x^2 + 2c_3 xy + c_2 y^2)} dx dy. \quad (14)$$

Unfortunately, no simpler analytical expressions are available for truncated Gaussian integrals contrary to non truncated Gaussian integrals. Also,

$$J_{x^i y^j} = N_{x^i y^j} - M_{x^i y^j} \quad (15)$$

where

$$N_{x^i y^j} = \int_{-\infty}^{\infty} \int_{-\infty}^{\infty} x^i y^j e^{-(c_1 x^2 + 2c_3 xy + c_2 y^2)} dx dy. \quad (16)$$

and

$$M_{x^i y^j} = \int \int_T x^i y^j \exp\left(-\left(c_1 x^2 + 2c_3 xy + c_2 y^2\right)\right) dx dy, \quad (17)$$

with $T = (-\infty; -a + u_x] \cup [a + u_x; +\infty) \times (-\infty; -b + u_y] \cup [b + u_y; +\infty)$. $N_{x^i y^j}$ is the integral over the entire domain for which analytical expressions are available in [19] and in Appendix F. Therefore, it is enough to compute the *surplus* $M_{x^i y^j}$:

$$M_{x^i y^j} = \int_{-a}^a \int_{[-\infty; -b] \cup [b; +\infty]} x^i y^j \exp(- (c_1 x^2 + 2c_3 xy + c_2 y^2)) dx dy, \quad (18)$$

While no analytical expressions are available for $M_{x^i y^j}$, we propose the following upperbound. The surplus is centered with respect to the origin leading to a second order error in the calculation. Using the symmetry $f_{i,j}(x, y) = f_{i,j}(-x, -y)$, and adding $\int_a^\infty \int_b^\infty f_{i,j}(x, y) dx dy + \int_a^\infty \int_{-\infty}^{-b} f_{i,j}(x, y) dx dy + \int_{-\infty}^{-a} \int_b^\infty f_{i,j}(x, y) dx dy + \int_{-\infty}^{-a} \int_{-\infty}^{-b} f_{i,j}(x, y) dx dy > 0$ (since $i + j$ is even), the surplus is bounded by :

$$M_{x^i y^j} \leq \tilde{M}_{x^i y^j}, \quad (19)$$

with

$$\begin{aligned} \tilde{M}_{x^i y^j} &= 2 \int_{-\infty}^{-a} \int_R x^i y^j e^{-(c_1 x^2 + 2c_3 xy + c_2 y^2)} dx dy \\ &\quad + 2 \int_R \int_{-\infty}^{-b} x^i y^j e^{-(c_1 x^2 + 2c_3 xy + c_2 y^2)} dx dy. \end{aligned} \quad (20)$$

If a and b are large relative to $\sqrt{\frac{c_2}{D}}$ and $\sqrt{\frac{c_1}{D}}$, Eq. 19 gets close to equality so $\tilde{M}_{x^i y^j}$ can be used instead of $M_{x^i y^j}$. Since we overestimate the *surplus* $M_{x^i y^j}$, the Fisher information is underestimated. As a result the variance is overestimated. The advantage of using $\tilde{M}_{x^i y^j}$ over $M_{x^i y^j}$ is that the integrals have exact analytical expressions in $\tilde{M}_{x^i y^j}$. For instance \tilde{M}_{x^2} can be computed directly, as outlined in Appendix D and Appendix E.

Once all the $J_{x^i y^j}$ are computed, the Fisher information matrix is computed using Eq. 9 and Appendix C.

3.2. Marginalization over the nuisance parameters

Since only the position variances of x_0, y_0 are of interest, it is beneficial to compute the marginalized distribution over the nuisance parameters A, c_1, c_2 and c_3 , that are respectively the amplitude and shape parameters of the object

image. Assuming the ML estimator is normally distributed with covariance matrix K , the marginalized Fisher information for x_0 and y_0 is [26]

$$F_{x_0, y_0}^{marg} = F_{x_0, y_0} - F_{[x_0, y_0], [A, c_1, c_2, c_3]} F_{A, c_1, c_2, c_3}^{-1} F_{[x_0, y_0], [A, c_1, c_2, c_3]}^T. \quad (21)$$

Eq. 21 shows that the presence of nuisance parameters leads to a loss of information as $F_{x_0, y_0}^{marg} \leq F_{x_0, y_0}$. Components of $F_{[x_0, y_0], [A, c_1, c_2, c_3]}$ are sums of the form $\sum x_n^i y_m^j \exp(-c_1 x_n^2 - c_2 y_m^2 - 2c_3 x_n y_m)$, for which $i + j$ is odd. It has been shown (see Eq.13) that the later sums are of the same order as $u_x \exp\left(-\frac{a^2 D}{c_2}\right)$. It follows therefore that every component of $F_{[x_0, y_0], [A, c_1, c_2, c_3]} \times F_{A, c_1, c_2, c_3}^{-1} \times F_{[x_0, y_0], [A, c_1, c_2, c_3]}^T$ is of the same magnitude as $u_x^2 \exp\left(-2\frac{a^2 D}{c_2}\right)$. Therefore, the contribution of the nuisance parameters in the Fisher information is extremely small and will be neglected.

Taking the inverse of $F_{x_0, y_0} \simeq F_{x_0, y_0}^{marg}$, the Rao Cramer lower bound has the following form:

$$K_{x_0, y_0} = \begin{bmatrix} \frac{2\sigma^2(c_1 c_2 \sqrt{\pi} - 2D\sqrt{\frac{D}{c_1}} bd_b)c_2}{Q} & -\frac{2c_3 c_1 c_2 \sigma^2}{Q} \\ -\frac{2c_3 c_1 c_2 \sigma^2}{Q} & \frac{2\sigma^2(c_1 c_2 \sqrt{\pi} - 2D\sqrt{\frac{D}{c_2}} ad_a)c_1}{Q} \end{bmatrix}. \quad (22)$$

With σ^2 being the signal variance and

$$Q = \sqrt{\pi} A^2 \sqrt{D} \left(4 \frac{D^2}{\sqrt{c_2 c_1}} ad_a bd_b - 2c_1 c_2 \left(\sqrt{\frac{D}{c_2}} ad_a + \sqrt{\frac{D}{c_1}} bd_b \right) + c_1 \pi c_2 \right) \delta_x \delta_y, \quad (23)$$

$d_a = \exp\left(-\frac{Da^2}{c_2}\right)$ and $d_b = \exp\left(-\frac{Db^2}{c_1}\right)$. In order to further simplify Eq. 22, it is convenient to introduce the signal to noise ratio of the brightest pixel as defined in [23]. Under the assumptions used to derive Eq 26, it can be written as:

$$\frac{S_b}{N} = \frac{A \exp(-\frac{1}{2}(c_1 u_x^2 + 2c_3 u_x u_y + c_2 u_y^2)) \delta_x \delta_y}{\sigma}, \quad (24)$$

where u_x and u_y were previously defined as the minimum distance between the center of the Gaussian surface and the center of a pixel for a given signal. Note that Eq. 24 does not take into account the pixel integration. It is possible

to average u_x and u_y as in the derivation of the Rao Cramer Lower Bound, however, to simplify u_x and u_y are set to zero. Hence, Eq. 24 becomes:

$$\frac{S_b}{N} = \frac{A\delta_x\delta_y}{\sigma}, \quad (25)$$

and keeping only first order terms Eq. 22 becomes :

$$K_{x_0, y_0} = \frac{\delta_x\delta_y}{(S_b/N)^2\sqrt{D}\pi^{3/2}} \times \begin{bmatrix} 2c_2 \left(\sqrt{\pi} + 2\sqrt{\frac{D}{c_2}}ad_a + 2\sqrt{\frac{D}{c_1}}\rho^2bd_b \right) & -2c_3 \left(\sqrt{\pi} + 2\sqrt{\frac{D}{c_2}}ad_a + 2\sqrt{\frac{D}{c_1}}bd_b \right) \\ -2c_3 \left(\sqrt{\pi} + 2\sqrt{\frac{D}{c_2}}ad_a + 2\sqrt{\frac{D}{c_1}}bd_b \right) & 2c_1 \left(\sqrt{\pi} + 2\sqrt{\frac{D}{c_1}}bd_b + 2\sqrt{\frac{D}{c_2}}\rho^2ad_a \right) \end{bmatrix}, \quad (26)$$

where $\rho = \frac{c_3}{\sqrt{c_1c_2}}$ is a correlation factor between the x and y-axis. It defines the orientation of the (elongated) Gaussian with respect to the pixel grid. Coefficients c_1 and c_2 are parameters of the fitted Gaussian curve that quantify the size of the signal in x and y direction while c_3 accounts for the orientation of the signal with respect to the axes. Variable A is the intensity of the brightest pixel and D is defined as $D = c_1c_2 - c_3^2$. Fig.4 illustrates the elongated object image with a rotation relative to the axis and a round object image. It has to be noted that in the observation of unknown objects without a priori information object images appear elongated with a relative motion relative to the sensor and is in general not aligned with the pixel grid. Stars, on the other hand, are often aligned with the pixel grid and have elongated, but non-rotated images. In this paper, we take the most general case. In this paper the elongated signal is represented via a non-symmetric Gaussian; other models, that more closely match very long streaked images (relative to the pixel size), are based on the convolution of a Gaussian with a rectangle [29, 30]. $d_a = \exp\left(-\frac{Da^2}{c_2}\right)$ and $d_b = \exp\left(-\frac{Db^2}{c_1}\right)$ account for the truncation of the signal. If the complete object image is sampled with infinite frame bounds, d_b and d_a go to zero and the variance simplifies to the results developed in [19]. For actual observations, finite cropping has to be applied.

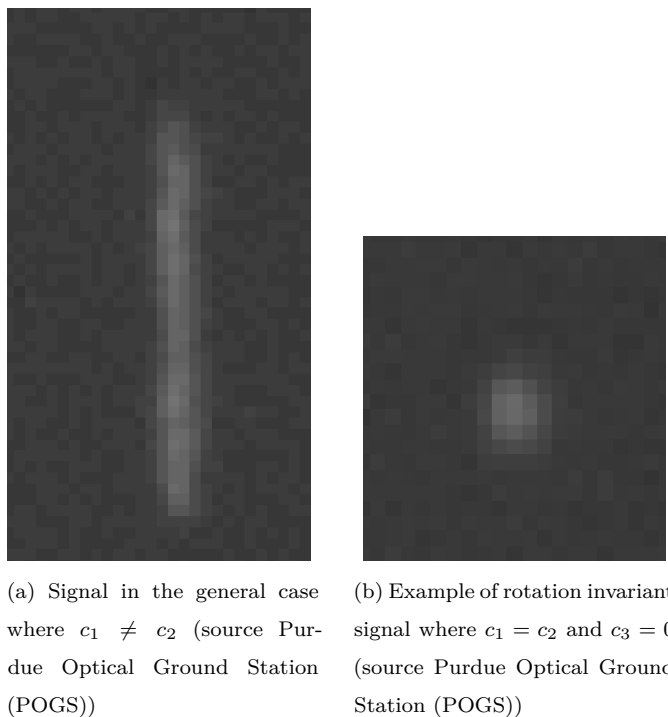


Figure 4: Signals received from an object.

If the signal is rotation invariant as in Fig 4b then $c_1 = c_2 = c$ and $c_3 = 0$ and Eq. 26 becomes:

$$K_{x_0, y_0} = \frac{\sigma^2}{A^2 \pi^{3/2}} \begin{bmatrix} 2(\sqrt{\pi} + 2\sqrt{cad_a}) & 0 \\ 0 & 2(\sqrt{\pi} + 2\sqrt{cbd_b}) \end{bmatrix}. \quad (27)$$

Introducing the signal to noise ratio as defined in Eq. 25, assuming square pixels and symmetrical cropping (ie. $a = b$) Eq. 27 becomes :

$$K_{x_0, y_0} = \frac{\delta^2}{\pi^{3/2} (S_b/N)^2} \begin{bmatrix} 2(\sqrt{\pi} + 2\sqrt{cad_a}) & 0 \\ 0 & 2(\sqrt{\pi} + 2\sqrt{cad_a}) \end{bmatrix}, \quad (28)$$

which is a completely symmetrical expression in the x and y direction.

3.3. Bayesian approach

As a comparison, a Bayesian approach is used to estimate the object's astrometric position. In this section, the joint distribution of the parameter θ

given a set of pixel value is derived using exactly the same assumptions made for deriving the RCLB. Using Bayes rule we have:

$$P(\theta|g_1 \dots g_{n_{\text{pix}}}) \propto P(\theta|g_1 \dots g_{n_{\text{pix}}})P(\theta) \quad (29)$$

with $P(\theta|g_1 \dots g_{n_{\text{pix}}})$ referring to the posterior distribution and $P(\theta)$ the prior distribution. The ML estimator does not include the notion of prior and therefore uniform priors are taken in the Bayesian analysis. The normalized distribution $\theta|g_1 \dots g_{n_{\text{pix}}}$ was computed using Metropolis-Hastings algorithm based on Monte Carlo Markov Chain (MCMC). Our implementation follows the algorithm presented in [31].

4. Method Comparison and Evaluation

4.1. Posterior Distribution

The Bayesian estimation allows to determine the distribution of the object image astrometric position even for small object images (under 5 pixels above the background level). Fig 5 shows the distribution of y_0 for an object image composed of 4 pixels.

Since the distribution shown in Fig. 5 is symmetrical with a fast decay of its tails it seems sufficient to know the first two moments of the distribution to accurately represent the probability density function of the astrometric position estimate from the object image. Further computations for larger signals show that the astrometric distribution becomes more Gaussian as the number of integrated pixels increases, in agreement with MLE theory [28]. It is hence sufficient to merely consider the variance to adequately quantify the uncertainty in the center location.

4.2. Validation

The different methods for evaluating the variance in the object image center on the pixel frame are compared. The first method is the simplified method

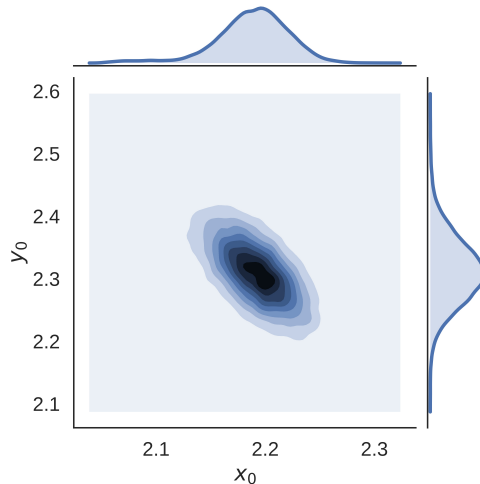


Figure 5: Joint distribution of x_0 and y_0 for a 4 pixel signal

developed in [19] using the RCLB under the limiting assumptions that the image center lies in the middle of a pixel and that an infinite amount of pixels is available. The second and third methods are the improved method to compute the RCLB introduced in this paper. One is the direct numerical evaluation of the RCLB as the inverse of the Fisher information matrix given in Appendix C and denoted as *exact lower bound* in the figures while the other one is our analytic approximate expression, derived in Eq.26 and denoted as *approximate lower bound* in the figures. Finally, the Bayesian estimation is fully numerical using the Metropolis-Hastings algorithm [32] implementation based on MCMC [31, 33]. The MCMC method is by far more computationally demanding than previous methods since the posterior distribution is constructed using 100 000 samples. In contrast, the numerical computation of the exact RCLB is straightforward as it merely requires the numerical inversion of a 6 by 6 matrix. The expression from [19] and the RCLB that has been derived in this paper are fully analytical expressions and are hence the fastest to compute.

As ground truth, a Monte Carlo simulation is used with 1 000 000 samples for the SNR=30 case and 100 000 samples for the SNR=5 case. Note that for

the SNR=5 case with narrow signals, the likelihood presents several maxima. In order to find a good maximum, the Newton method is initialized several times for each case. For comparison, a centroid method is implemented. As described in Appendix G, the centroid is not equivalent to the Gaussian fitting but is more commonly used for small signals. The results for two different noise levels, SNR=30 and SNR=5 (relative to the brightest pixel) are shown in Figs. 6 and 7, as a function of the full width at the half maximum (FWHM) of the object image of the true object image. The variance is given in pixels².

4.2.1. Results of the tests for different signal sizes and SNR

In general, the Bayesian approach and the MC verification differ for small signals as it can be seen in Fig. 6. This is due to the theoretical difference between the Bayesian framework and the MC verification. In both cases, the object image has been cropped at four standard deviations in x direction and five standard deviations in the y direction in order to simulate unsymmetrical cropping. The noise is assumed to be constant over this cropped sub-frame. For example, if the standard deviation of the fitted Gaussian is 5 pixels in the x and y directions, in our test case the cropped image will be centered around the signal, 40 pixels large in the x direction and 50 pixels wide in y direction. More precisely, the Gaussian curve parameters are $a = 4\sigma_x, b = 5\sigma_x, c_1 = 1/\sigma_x^2, c_2 = 1/\sigma_y^2$ and $c_3 = \frac{1}{\sigma_x\sigma_y}$. It can be seen that the approximation of the RCLB according to [19] constantly underestimates the variance even for very large signals, and is hence overconfident. On the other hand, our improved method captures the cropping effect well and follows the exact lower bound well. Even for large signals, the *Hagen estimation* constantly underestimate the center variance of about 15 % even for a signal where only 2.5 % of the intensity has been cut. This bias comes from the truncation effects that are not considered in [19] and that have a significant effect in this set of tests. By assuming that the entire signal is sampled, the estimation from [19] overestimates the amount of information available and underestimates the signal center variance. This remark justifies the use of our more accurate expression designed for cropped signal, even when

the signal almost completely sampled. This gain in accuracy comes from the less restrictive set of assumptions we use to derive our expressions of the center variance.

Although theory states that the Rao Cramer Lower Bound underestimates the variance of the ML estimator, Fig. 6 and 7 show that in practice the RCLB is reached even for object images with very small FWHM and low signal to noise ratios. Consequently, even for small signals (FWHM e.g 10 pixels) the approximate RCLB defined in Eq. 26 is a good estimation of the variance. This remark is all the more true that the SNR is high.

For SNR=5 (see fig. 7), contrary to the high SNR case, the exact RCLB underestimates the estimator variance with respect to the Bayesian approach and the MC validation, especially for small signals. As for the previous case our analytical formulation outperforms previous analytical estimations. Unsurprisingly, for those cases the variance sharply increases, as more and more information is lost into one pixel. For low SNR, the RLCB (exact or our estimation) is only valid for signals with FWHM greater than 3 pixels. The centroid method only used as an illustration in this case where the Gaussian fitting is challenging to use features a higher variance than the Gaussian fitting. This test is indeed favorable to the Gaussian fitting method since the numerically generated signals are noisy Gaussian signals. This test also illustrates the differences between the Bayesian approach and the MC verification. When the signals are small, the two methods do not provide equivalent uncertainty estimates. In our case, the MC consistently predicts a higher variance than the Bayesian approach.

4.2.2. Effect of truncation in the center variance

In actual observations, it is never the case that the theoretically infinite signal is sampled but only a finite pixel frame is available. The infinite support of the signal comes from the fact that the object image is a diffraction pattern. Furthermore, the image frame shows several sources besides the object image of interest; other objects and most prominently stars, which each constitute a

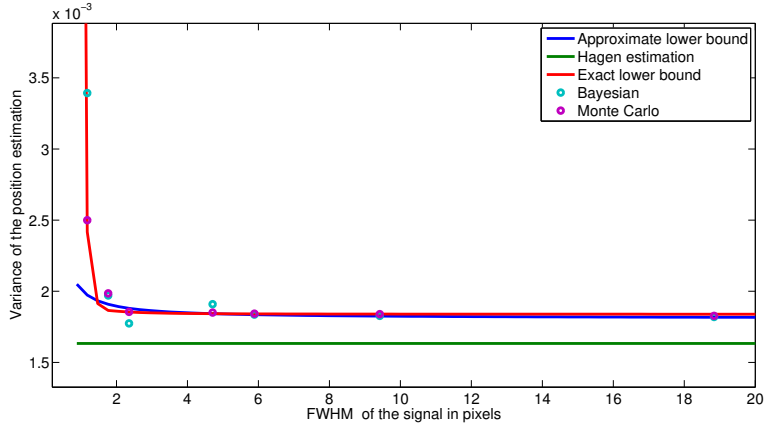


Figure 6: Convergence of the ML position estimation variance as a function of the FWHM for generated signal with SNR=30

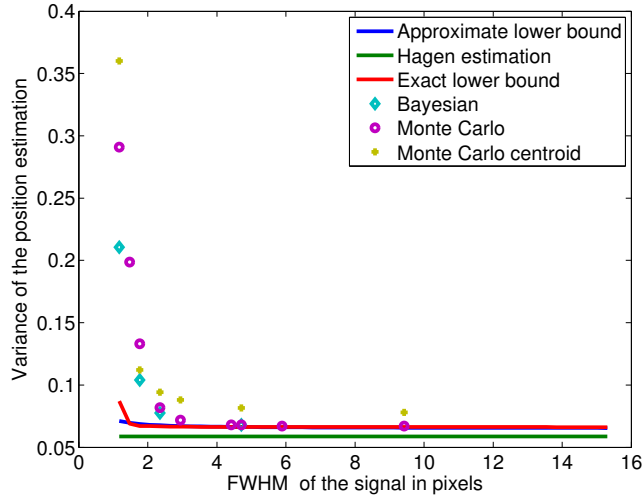


Figure 7: Convergence of the ML position estimation variance as a function of the FWHM for generated signal with SNR=5

diffraction pattern of their own. In actual image processing, hence, a relatively tight area around the part of the object image that is clearly above the background is used for centroiding.

The improved accuracy of the center estimation, when not the entire signal

can be sampled is illustrated via a direct comparison to [20, 19]. we study the evolution of the center variance with the percentage of signal that is truncated. We consider a square grid. The standard deviation of the signal is 8 pixel in both x and y-direction, the grid size goes from 22 by 22 pixels where 69 % of the signal is sampled to a grid size of 40 by 40 where 99.65 % of the signal is sampled. The results are summarized in figure 8 where we compare *Hagen estimation*, our analytical estimation (*Approximate lower bound*), the exact lower bound estimated numerically (*Exact Lower Bound*) and a Monte Carlo validation carried out on 100 000 samples. As already shown in [19], the exact RCLB is able to accurately approximate the MC estimation of the center variance. In particular, it outperforms the approximate analytical expressions derived in this work and in [19]. The Hagen approximation is unadapted to capture the information loss due to truncation while our approximation is able to capture the qualitative trend. In terms of relative error, we observe that Hagen estimation features an error of 7 % while our estimate features an error of 1.2 % when 88 % of the signal is sampled. When only 70 % of the signal is sampled, Hagen estimation is off by 32 % whereas our estimation is 11 % off compared to MC results. Hence we recommend using the expressions derived in this work for cases where 85-90 % of the signal is sampled. In any case, our estimate outperforms analytical expressions found in the literature. If less than 85 % of the signal is sampled, using the numerical exact RCLB can bring a significant gain in accuracy. When possible, it can be of interest to predict the expected precision loss in the center position estimation when the signal is truncated in order to set up the right aperture size. One can look at the amount of signal that is truncated but a more sensible quantity to look at is the Fisher information repartition per pixels. The Fisher information quantifies the amount of information available, per pixels to estimate the Gaussian curve parameters. From paragraph 3.2, the variance in the center position is mostly due to F_{x_0,x_0}, F_{y_0,y_0} and F_{x_0,y_0} . In fig 9b is represented $A^2 R_{n,m} ((c_1 \xi_n)^2 + (c_2 \eta_m)^2)$ which represents repartition of $F_{x_0,x_0} + F_{y_0,y_0}$ used estimate the center position in the case where $c_3 = 0$. For comparison, the corresponding noiseless signal is represented in Fig 9a. We

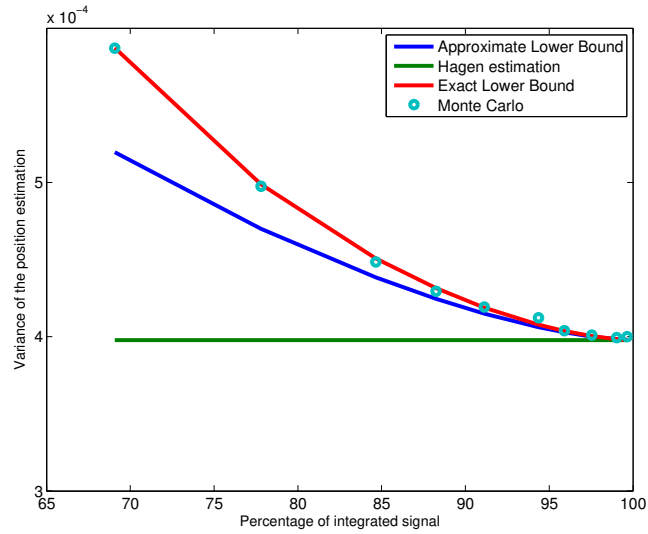
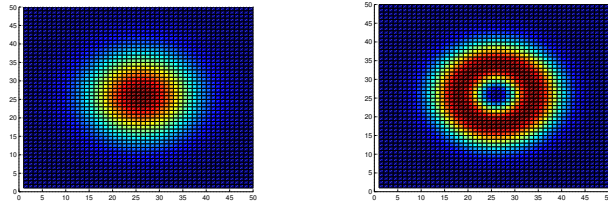


Figure 8: Evolution of the center variance function of the signal truncation level



(a) Noiseless symmetrical signal (b) Fisher information density

Figure 9: Noiseless signal and the Fisher information associated with the center position estimation

see that the pixels that help the most to estimate the position of the centers are not the brightest ones located in the center of the signal but they form a ring around the most signal. As a consequence, when truncating the signal one should try to minimize Fisher information that is removed rather than the amount of signal that is removed. Note that this analysis is only valid when the signal is cropped symmetrically. Otherwise, the results from paragraph 3.2 are not valid anymore.

Using the results derived in the previous section, one can instantaneously estimate the uncertainty in the position of a space object without simulating object image frames or actually doing Gaussian fits. In Appendix B, a lookup table gives the variance of the center position given the signal-to-noise ratio, the number of pixels above half the brightest pixel intensity (FWHM) and the ratio of the length of the signal in the longest direction over the length in the shortest direction counting pixels above half the brightest pixel intensity.

4.2.3. Influence of the pixel scale on the center variance

Being able to predict the uncertainty in astrometric position also helps to gain insight on how pixel resolution and size of the signal affects the uncertainty in the object astrometric position. In this section, we propose two experiments. The first one investigates the influence of the pixel resolution for four different signals at constant SNR (see eq 25 and noise level). The second one illustrates the influence pixel resolution while keeping the integrated intensity and noise constant. This second test objective is to suggest an optimal pixel resolution for a given observation scenario

First test. The signal main characteristics are reported in table 1. Fig 11 shows how the pixel resolution influences the uncertainty in signal location for four different signals shown in Fig. 10. The first signal is contained only in a few pixels with a high SNR, the second signal spreads over a large number of pixels with the same high SNR. The third has the same shape as the first signal but the SNR here is lower. The fourth one is as large as the second one but with a low SNR. Note that for all signals the maximum amplitude is kept constant so that signals 2 and 4 contain on average 4 times more signal intensity than signals 1 and 3 but spread over a larger number of pixels. According to Fig.11 representing the evaluation of the standard deviation of the signal position function of the pixel resolution, large signals (signal 3 and 4) are less accurate than smaller ones (signal 1 and 2) despite the fact that they integrate more photons. In our case, the small low SNR (signal 2) still has a lower variance than signal 3 although there are more pixels to fit and less noise in signal 3. Note that the signal sizes

Table 1: Signal characteristics

Signal	A	c_1	c_2	c_3	Integrated volume [<i>pixel</i>] ²
Signal 1	100	0.8	0.4	0.2	1167
Signal 2	100	0.8	0.4	0.2	1167
Signal 3	100	0.15	0.15	0	4188
Signal 4	100	0.15	0.15	0	4188

are selected large enough such that the RCLB is reached and our expressions valid. For significantly smaller signals, a Bayesian approach should be preferred.

Second test. In this test, we consider one observation scenario and we vary the pixel scale. In this case, the integrated Gaussian should be kept constant. In the case of a symmetrical signal, we have $V = \frac{2\pi A}{c}$ constant. Hence we see that the SRN as defined in 25 decreases as the signal width increases at a constant V . According to eq. 28 the variance scales like $1/c^2$ or $1/c^{3/2}$ if the signal is truncated. Therefore our estimation asserts that the smaller the signal, the lower the variance. Unfortunately for narrow signals, the formulae are not applicable because they significantly underestimate the actual center variance, therefore they should not be used to find the optimal pixel scale. Using the exact RCLB and taking into account the integration bias, [21] shows that there is an optimal pixel scale. Fig. 12 illustrates the trend predicted by our estimates where the variance tends to decrease as the signal width increases. The results are obtained with a symmetrical signal.

4.3. Comparison with Rule of Thumb

A rule of thumb is often used in astronomy to roughly quantify the uncertainty in astrometric location. It defines the variance in astrometric position as:

$$\widetilde{K}_x = \frac{1}{(FWHM_x \times S/N)^2}, \quad (30)$$

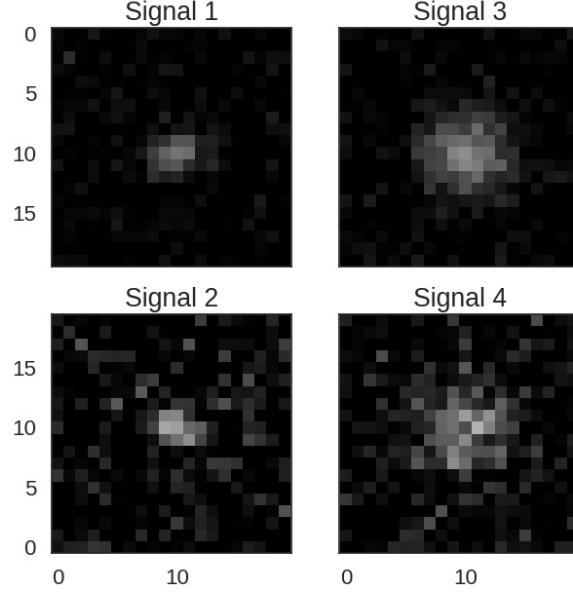


Figure 10: Example of Space object signals: signal 1 represents a small high SNR example, signal 2 is a small low SNR example, signal 3 represents a large high SNR example and signal 4 is a large low SNR example.

with an equivalent expression for the y axis. To compare it with the expressions derived in this work, we propose to approximate \widetilde{K}_x function of the Gaussian curve parameter. For simplicity, we consider the round signal with scale parameter c . The signal to noise ratio defined as

$$SNR = \frac{\sum_i S_i}{\sum_i N_i}, \quad (31)$$

where S_i is the signal intensity and N_i is the noise. Replacing sums with integrals we get $\sum_i S_i \simeq \frac{A\pi}{c}$. We propose to integrate the constant noise over three standard deviations of the Gaussian signal such that $\sum_i N_i \simeq \frac{9\sigma\pi}{c}$. Finally the SNR scales as

$$SNR \simeq \frac{A}{9\sigma}. \quad (32)$$

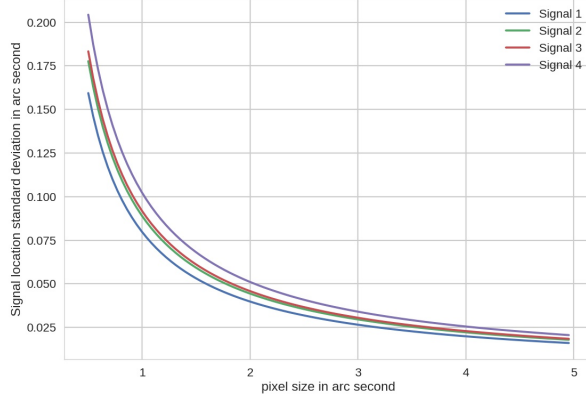


Figure 11: Evolution of center variance with the resolution of the CCD for the signals shown on Fig 10.

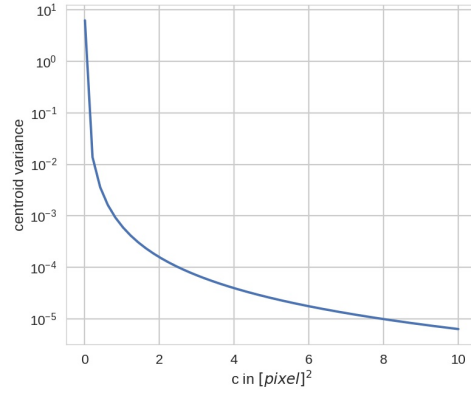


Figure 12: Evolution of the signal center variance with the signal width at constant integrated volume

Taking $FMWHM = 2.55 \frac{1}{\sqrt{c}}$, we get for the rule of thumb :

$$\widetilde{K}_x \simeq \frac{9c}{2.55(S_b/N)^2}, \quad (33)$$

For Gaussian signals and constant noise, the rule of thumb, as it is defined in this work, captures the dependencies in the SNR well but fails to account for the influence of the signal geometry on the variance. Clearly the rule of thumb

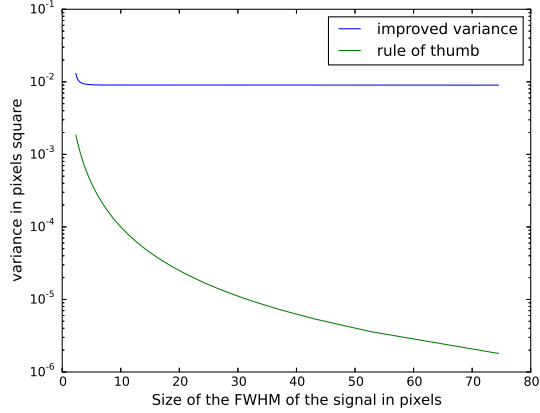


Figure 13: Comparison of the rule of thumb with our estimation of variance for different signal sizes.

scales as c whereas our expression (and [20, 19]) do not have such dependency. In Fig. 13, the variances are computed with a constant signal to noise ratio of ten, and for different object image sizes of constant FWHM. Note that the total signal intensity is not kept constant in this case. The results clearly show that the rule of thumb underestimates the uncertainty in the astrometric position in any practical situations ie. as soon as the object image is larger than two or three pixels. The rule of thumb also wrongly goes to zero as the signal size increases, which contradicts the Monte Carlo simulations obtained in Fig. 6.

5. Conclusions

As signal generation is a stochastic process, the identical incoming signal from an object leads to different object image representations. Each of the representations leads to a different center estimate. The center is furthermore dependent on the signal to noise ratio and the pixel size relative to the spread of the object image in pixels. To efficiently quantify the variation in the center estimates, this paper derives rigorous expressions to compute the variance of the extracted center, using the Rao Cramer lower bound (RCLB). While previous work has been shown to consistently underestimate the variance because of

simplifying assumptions, in this work, improved analytic expressions for the variance have been derived. The obtained expressions depend on the signal to noise, the pixel size and the size of the object signal relative to the pixels have been derived. The new expressions can be used even when a limited number of pixels are clearly above the background level whereas the expressions available in the literature can only be used when the signal is not truncated. Furthermore, we do not assume that the object image true center is at the center of any single pixel of the pixel grid. The new expressions allow for fast computation of the variance. The derived expressions have been compared to a Bayesian evaluation using Markov Chain Monte Carlo (MCMC) method in the Metropolis-Hastings implementation and a reference Monte Carlo estimation. The MCMC implementation is computationally intensive and performs similarly to the numerical evaluation of the RCLB and the analytical expression of the RCLB that has been derived in this paper albeit at much lower computational cost. Only when the full width of half maximum of the object signal is small as 4 pixels per FWHM does the Bayesian MCMC approach show advantages. Note that in most cases the simple analytical expressions derived in this work compare very well to Bayesian and Monte Carlo calculations

In particular, the domain of validity of the Gaussian noise assumption has been delimited. Using a Bayesian approach, it is shown that the distribution of the position estimation is well described by its first two moments. This result justifies the use of only the covariance matrix to quantify the uncertainties under consideration.

Using the derived analytical expressions, it has been shown that the observation likelihood can be computed analytically, solely based on the deterministic aspect of the observation process without expensive Monte Carlo simulations or other numerical procedures.

For practical purposes, a simple shorthand lookup table has been created with precomputed variances.

Acknowledgement

The authors would like to thank Dr Emmanuel Delande for his advice on Bayesian estimation and maximum likelihood estimation. We would like to acknowledge the support of this work via FA9550-14-1-0348 DEF.

- [1] S. B. Howell, Handbook of CCD Astronomy, Cambridge University Press, 2006. doi:10.2277/0521617626.
- [2] J. R. Janesick, T. Elliott, S. Collins, M. M. Blouke, J. Freeman, Scientific charge-coupled devices, 1987. doi:10.1117/12.7974139.
- [3] W. J. Merline, S. B. Howell, A realistic model for point-sources imaged on array detectors: The model and initial results, *Experimental Astronomy* 6 (1-2) (1995) 163–210. doi:10.1007/BF00421131.
- [4] I. Smal, M. Loog, W. Niessen, E. Meijering, Quantitative comparison of spot detection methods in fluorescence microscopy, *IEEE Transactions on Medical Imaging*, 29 (2) (2010) 282–301.
- [5] B. Zhang, J. Zerubia, J.-C. Olivo-Marin, Gaussian approximations of fluorescence microscope point-spread function models, *Applied Optics* 46 (10) (2007) 1819–1829.
- [6] P. Massey, G. H. Jacoby, CCD Data: The Good, The Bad, and The Ugly, in: Steve B. Howell (Ed.), *Astronomical CCD observing and reduction techniques*, Vol. 23, Astronomical Society of the Pacific, San Francisco, 1992, p. 240.
- [7] R. P. S. Mahler, *Statistical Multisource-Multitarget Information Fusion*, Artech House, Inc., Norwood, MA, USA, 2007.
- [8] K. J. DeMars, I. I. Hussein, C. Frueh, M. K. Jah, R. Scott Erwin, Multiple-Object Space Surveillance Tracking Using Finite-Set Statistics, *Journal of Guidance, Control, and Dynamics* (2015) 1–16.

- [9] E. Delande, C. Frueh, J. Houssineau, D. Clark, Multi object filtering for space situational awareness, AAS Space Flight Mechanics Meeting, Williamsburg, 2015.
- [10] J. S. McCabe, K. J. DeMars, C. Frueh, Integrated Detection and Tracking for Multiple Space Objects, in: AAS Space Flight Mechanics Meeting, Williamsburg, 2015.
- [11] B. E. A. Saleh, Estimation of the Location of an Optical Object with Photodetectors Limited by Quantum Noise, *Appl. Opt.* 13 (8) (1974) 1824–1827. doi:10.1364/AO.13.001824.
- [12] T. Delabie, J. D. Schutter, B. Vandebussche, An accurate and efficient Gaussian fit centroiding algorithm for star trackers, Space Flight Mechanics Meeting, Kauai, Hawaii, 2013.
- [13] A. Foi, M. Trimeche, V. Katkovnik, K. Egiazarian, Practical poissonian-gaussian noise modeling and fitting for single-image raw-data, *IEEE Transactions on Image Processing* 17 (10) (2008) 1737–1754. doi:10.1109/TIP.2008.2001399.
- [14] R. C. Stone, A comparison of digital centering algorithms, *Astronomical Journal* 97 (1989) 1227–1237.
- [15] R. Manish, Profile fitting in crowded astronomical images, Master’s thesis, School of Aeronautics and Astronautics, Purdue University (2015).
- [16] G. B. T. Schildknecht, U. Hugentobler, A. Verdun, CCD Algorithms for space debris detection, Tech. rep., University of Berne (1995).
- [17] H. Tiersch, S.B. Howell (ed.): Astronomical CCD observing and reduction techniques. Astronomical Society of the Pacific 1992, ASP Conference Series 23, 339 s., Preis: 55,-ISBN 0-937707-42-4, *Astronomische Nachrichten* 314 (6) (1993) 398. doi:10.1002/asna.2113140603.

- [18] C. Frueh, Identification of Space Debris, Shaker Verlag, Aachen, 2011, ISBN: 978-3-8440-0516-5.
- [19] N. Hagen, E. Dereniak, Gaussian profile estimation in two dimensions., Applied optics 47 (36) (2008) 6842–6851. doi:10.1364/AO.47.006842.
- [20] N. Hagen, M. Kupinski, E. Dereniak, Gaussian profile estimation in one dimension, Applied optics 46 (22) (2007) 5374–5383.
- [21] K. A. Winick, Cramer-Rao lower bounds on the performance of charge-coupled-device optical position estimators, JOSA A 3 (11) (1986) 1809–1815.
- [22] F. Sanson, C. Frueh, Noise Quantification in Optical Observations of Resident Space Objects for Probability of Detection and Likelihood, in: Proc. AIAA/AAS Astrodynamics Specialist Conference, Vail, Colorado, 2015.
- [23] F. Sanson, C. Frueh, Probability of detection in non-resolved images: Application to space object observation, Journal of Astronautical Sciences, submitted.
- [24] H. Barrett, C. Dainty, D. Lara, Maximum-likelihood methods in wavefront sensing: stochastic models and likelihood functions, JOSA A 24 (2) (2007) 391–414.
- [25] R. Savage, S. Oliver, Bayesian methods of astronomical source extraction, The Astrophysical Journal 661 (2) (2007) 1339.
- [26] V. P. Bhapkar, Conditioning on ancillary statistics and loss of information in the presence of nuisance parameters, Journal of Statistical Planning and Inference 21 (2) (1989) 139–160.
- [27] H. H. Barrett, K. J. Myers, Foundations of Image Science, Wiley Series in Pure and Applied Optics, Wiley, 2013.

- [28] A. Stuart, K. Ord, Kendall's Advanced Theory of Statistics: Volume 1: Distribution Theory, no. vol. 2; vol. 1994 in Kendall's Advanced Theory of Statistics, Wiley, 2009.
- [29] N. Houtz, C. Frueh, Streak detection and characterization in ground-based optical observations of space objects, 2018.
- [30] W. A. Dawson, M. D. Schneider, C. Kamath, Synthesis of disparate optical imaging data for space domain awareness, AMOS Advanced Maui Optical and Space Surveillance Technology Conference, Maui, Hawaii, 2016.
- [31] J. Kaipio, E. Somersalo, Statistical and Computational Inverse Problems, Vol. 160 of Applied Mathematical Sciences, Springer-Verlag, New York, 2005. doi:10.1007/b138659.
- [32] N. Metropolis, A. W. Rosenbluth, M. N. Rosenbluth, A. H. Teller, E. Teller, Equation of State Calculations by Fast Computing Machines, The Journal of Chemical Physics 21 (6) (1953) 1087. doi:10.1063/1.1699114.
- [33] P. Diaconis, The markov chain monte carlo revolution, Bulletin of the American Mathematical Society 46 (2) (2009) 179–205.
- [34] C. Frueh, M. Jah, Detection Probability of Earth Orbiting Objects Using Optical Sensors, in: Advances in the Astronautical Sciences, Hilton Head, 2014.

Nomenclature

A	Amplitude of the Gaussian
a	size of the frame considered for Gaussian fitting in x direction
B	Total intensity of the background pixels
b	size of the frame considered for Gaussian fitting in y direction
c_1	Gaussian parameter (cf Eq. A.1)
c_2	Gaussian parameter (cf Eq. A.1)

c_3	Gaussian parameter (cf Eq. A.1)
c	Gaussian parameter in the symmetrical case ($c = c_1 = c_2$)
D	Determinant ($D = c_1 c_2 - c_3^2$)
D_i	Signal of the dark noise in pixel i
$E_{n,m}$	$E_{n,m} = e^{(-\frac{1}{2}(c_1(x_n-x_0)^2+2c_3(x_n-x_0)(y_m-y_0)+c_2(y_m-y_0)^2))}$
erf	error function
F	Fisher information
$FWHM$	Full Width at Half Maximum
g_i	Intensity at pixel i
$f_{i,j}$	$f_{i,j}(x,y) = x^i y^j \exp(- (c_1 x^2 + 2c_3 xy + c_2 y^2))$
η_m	$\eta_m = y_m - y_0$
G	$G = Ae^{(-\frac{1}{2}(c_1(x_i-x_0)^2+2c_3(x_i-x_0)(y_i-y_0)+c_2(y_i-y_0)^2))}$
Γ	Gamma function
δ_x	pixel size on x direction
δ_y	pixel size on y direction
δ	pixel size square pixels
θ	vector of the Gaussian parameters ($A, c_1, c_2, c_3, x_0, y_0$)
θ_{true}	Actual value of the Gaussian parameters
θ_{MLE}	value of the Gaussian parameters estimated by the MLE
$J_{x^i y^j}$	$J_{x^i y^j} = \int_{-a+u_x}^{a+u_x} \int_{-b+u_y}^{b+u_y} x^i y^j \exp(- (c_1 x^2 + 2c_3 xy + c_2 y^2)) dx dy.$
K	Rao Cramer lower bound (inverse Fisher information)
\tilde{K}	center variance computed with the rule of thumb
L	Likelihood
l	log likelihood
$\lambda_{D,i}$	Poisson parameter of the random variable $S_{D,i}$
$\lambda_{\text{obj},i}$	Poisson parameter of the random variable $S_{\text{obj},i}$
$\lambda_{S,i}$	Poisson parameter of the random variable $S_{S,i}$
$\lambda_{\text{act},i}$	Poisson parameter of the random variable $S_{S,i} + S_{D,i} + S_{\text{obj},i}$
$\lambda_{b,d}$	$\lambda_{b,d} = \lambda_S + \lambda_D$
m	number of of sub-frames

μ_B	Mean estimated background
N	Total Noise
N_*	Total noise due to the object
$N_{x^i y^j}$	$N_{x^i y^j} = \int_{\mathcal{R} \in} x^i y^j \exp(- (c_1 x^2 + 2c_3 xy + c_2 y^2)) dx dy.$
n_B	Number of pixel used in background determination
n_{pix}	Number of signal pixel
ξ_n	$\xi_n = x_n - x_0$
S	Total Signal
S_b	intensity of the brightest pixel
S_*	Averaged total signal of the object
d_a	$d_a = \exp\left(\frac{-a^2 D}{c_2}\right)$
d_b	$d_b = \exp\left(\frac{-b^2 D}{c_1}\right)$
s	Gaussian curve
s_i	Gaussian curve evaluated at pixel i
σ	CCD noise with the Gaussian fitting
$M_{x^i y^j}$	the surplus defined Eq. 18
t	Detection threshold
T	integration interval $T = (-\infty; -a + u_x] \cup [a + u_x; +\infty)$ $\times (-\infty; -b + u_y] \cup [b + u_y; +\infty)$
Q	$Q = \sqrt{\pi} A^2 \sqrt{D} \left(4 \frac{D^2}{\sqrt{c_2 c_1}} a d_a b d_b - 2 c_1 c_2 \left(\sqrt{\frac{D}{c_2}} a d_a + \sqrt{\frac{D}{c_1}} b d_b \right) + c_1 \pi c_2 \right) \delta_x \delta_y$
U	Error associated to the CCD limited resolution
\mathcal{U}	uniform distribution
u_x	Offset in x direction of the signal center with respect to the pixel grid
u_y	Offset in y direction of the signal center with respect to the pixel grid
ρ	$\rho = \frac{c_3}{\sqrt{c_1 c_2}}$
x_0	center of the Gaussian on x direction
x_n	x coordinate of the m pixel
y_0	center of the Gaussian on y direction

y_m y coordinate of the m pixel

Appendix A. Maximum Likelihood center Estimation

The background subtracted object image signal pattern at the sensor (see Eq. 2) is fitted with a Gaussian curve. An example of Gaussian fitting applied to an actual signal is given in Fig. 3. For details see [34]. The actual position of the source can be retrieved under the assumption that it corresponds to the center of the fitted Gaussian curve on the pixel grid. This is in general not the center of any given pixel. More precisely, it is assumed that the fitted subspace has the following form

$$G = Ae^{(-\frac{1}{2}(c_1(x_i-x_0)^2+2c_3(x_i-x_0)(y_i-y_0)+c_2(y_i-y_0)^2))}, \quad (\text{A.1})$$

noting $\theta = (A, x_0, y_0, c_1, c_2, c_3)$ where A is the amplitude, x_0 and y_0 the center of the fitted Gaussian on the pixel grid and c_1 , c_2 and c_3 the coefficients of the inverse covariance matrix. The position of the object image on the pixel grid then is denoted by x_0, y_0 .

The maximum likelihood (ML) estimator has been widely used in Gaussian fitting of signals [19, 11, 21] for its good properties: it is an unbiased, consistent and asymptotically efficient estimator under mild assumptions [28]. Defining the likelihood of the set of parameters θ for a signal as:

$$L = P(S = G|\theta), \quad (\text{A.2})$$

then the maximum of likelihood is defined as:

$$\hat{\theta}_{MLE} = \operatorname{argmax}_{\theta} (P(S = G|\theta)). \quad (\text{A.3})$$

If the noise is Gaussian independent for two different pixels, the likelihood becomes:

$$L = \prod_i^{n_{\text{pix}}} \exp\left(-\frac{1}{2}\left(\frac{(S_i - G_i)^2}{\sigma_i^2}\right)\right). \quad (\text{A.4})$$

G_i is the Gaussian surface, Eq. A.1 and S_i signal at the i th pixel, defined in Eq.1. σ_i is the standard deviation of the noise distribution at pixel i . If the noise amplitude is assumed to be constant over the signal σ_i is constant and denoted σ in the rest of this article. Then the log likelihood, also called the score is:

$$l = - \sum_i^{n_{\text{pix}}} \frac{(S_i - G_i(\theta))^2}{2\sigma^2}. \quad (\text{A.5})$$

Appendix B. Lookup Table

The following tables can be used to directly estimate the uncertainty in the signal astrometric position for a specific observation setting. $\frac{S_b}{N}$ is the signal to noise ratio of the brightest pixel, FWHM x corresponds to the FWHM along the x direction and FWHM y along the y direction. Once those quantities have been determined the lookup table gives the variance in the astrometric position. If needed additional values can be generated using 27. The following table was obtain simulating Gaussian signal with fixed maximum intensity of 1000 electrons and gain of 2. To obtain different values of signal-to-noise the background level varied between 10 and 1000 electrons and the readout noise varied between 0.2 to 150 ADU.

Table B.2: LOOKUP TABLE for OBJECT ASTROMETRIC POSITION VARIANCE

$\frac{S_b}{N}$	FWHM x	FWHM y	Variance in $x \times \frac{\delta^2}{(S/N)^2}$	Variance in $y \times \frac{\delta^2}{(S/N)^2}$	Covariance $\times \frac{\delta^2}{(S/N)^2}$
20.384705	10.531880	10.531880	129.180196	129.176305	-0.776914
20.393602	3.980677	10.531880	18.198596	18.393586	-0.110362
20.394506	2.921018	10.531880	9.796892	9.901762	-0.059411
20.394879	2.416179	10.531880	6.702544	6.774266	-0.040646
20.394970	2.106376	10.531880	5.093700	5.148196	-0.030889
9.109910	10.531880	10.531880	129.180196	129.176305	-0.776914
9.116150	3.980677	10.531880	18.198596	18.393586	-0.110362
9.116785	2.921018	10.531880	9.796892	9.901762	-0.059411
9.117046	2.416179	10.531880	6.702544	6.774266	-0.040646
9.117110	2.106376	10.531880	5.093700	5.148196	-0.030889
5.379920	10.531880	10.531880	129.180196	129.176305	-0.776914
5.383823	3.980677	10.531880	18.198596	18.393586	-0.110362
5.384219	2.921018	10.531880	9.796892	9.901762	-0.059411
5.384383	2.416179	10.531880	6.702544	6.774266	-0.040646
5.384423	2.106376	10.531880	5.093700	5.148196	-0.030889
3.782134	10.531880	10.531880	129.180196	129.176305	-0.776914
3.784920	3.980677	10.531880	18.198596	18.393586	-0.110362
3.785203	2.921018	10.531880	9.796892	9.901762	-0.059411
3.785319	2.416179	10.531880	6.702544	6.774266	-0.040646
3.785348	2.106376	10.531880	5.093700	5.148196	-0.030889
2.909595	10.531880	10.531880	129.180196	129.176305	-0.776914
2.911750	3.980677	10.531880	18.198596	18.393586	-0.110362
2.911969	2.921018	10.531880	9.796892	9.901762	-0.059411
2.912060	2.416179	10.531880	6.702544	6.774266	-0.040646
2.912082	2.106376	10.531880	5.093700	5.148196	-0.030889

Appendix C. Fisher Information

The exact expression for the Fisher information as derived in [19] is:

$$\begin{aligned}
F_{11} &= \sum_{n=0, m=0}^{n_{\text{pix}}} R_{n,m} \\
F_{12} &= A \sum_{n=0, m=0}^{n_{\text{pix}}} R_{n,m} (c_1 \xi_n + c_3 \eta_m) \\
F_{13} &= A \sum_{n=0, m=0}^{n_{\text{pix}}} R_{n,m} (c_2 \eta_m + c_3 \xi_n) \\
F_{14} &= -\frac{A}{2} \sum_{n=0, m=0}^{n_{\text{pix}}} R_{n,m} \xi_n^2 \\
F_{15} &= -\frac{A}{2} \sum_{n=0, m=0}^{n_{\text{pix}}} R_{n,m} \eta_m^2 \\
F_{16} &= -A \sum_{n=0, m=0}^{n_{\text{pix}}} R_{n,m} \xi_n \eta_m \\
F_{22} &= A^2 \sum_{n=0, m=0}^{n_{\text{pix}}} R_{n,m} (c_1 \xi_n + c_3 \eta_m)^2 \\
F_{23} &= A^2 \sum_{n=0, m=0}^{n_{\text{pix}}} R_{n,m} (c_2 \eta_m + c_3 \xi_n) (c_1 \xi_n + c_3 \eta_m) \\
F_{24} &= -\frac{A^2}{2} \sum_{n=0, m=0}^{n_{\text{pix}}} R_{n,m} \xi_n^2 (c_1 \xi_n + c_3 \eta_m) \\
F_{25} &= -\frac{A^2}{2} \sum_{n=0, m=0}^{n_{\text{pix}}} R_{n,m} \eta_m^2 (c_1 \xi_n + c_3 \eta_m) \\
F_{26} &= -A^2 \sum_{n=0, m=0}^{n_{\text{pix}}} R_{n,m} \xi_n \eta_m (c_1 \xi_n + c_3 \eta_m) \\
F_{33} &= A^2 \sum_{n=0, m=0}^{n_{\text{pix}}} R_{n,m} (c_2 \eta_m + c_3 \xi_n)^2 \\
F_{34} &= -\frac{A^2}{2} \sum_{n=0, m=0}^{n_{\text{pix}}} R_{n,m} \xi_n^2 (c_2 \eta_m + c_3 \xi_n)
\end{aligned}$$

$$\begin{aligned}
F_{35} &= -\frac{A^2}{2} \sum_{n=0, m=0}^{n_{\text{pix}}} R_{n,m} \eta_m^2 (c_2 \eta_m + c_3 \xi_n) \\
F_{36} &= -A^2 \sum_{n=0, m=0}^{n_{\text{pix}}} R_{n,m} \xi_n \eta_m (c_2 \eta_m + c_3 \xi_n) \\
F_{44} &= \frac{A^2}{4} \sum_{n=0, m=0}^{n_{\text{pix}}} R_{n,m} \xi_n^4 \\
F_{45} &= \frac{A^2}{4} \sum_{n=0, m=0}^{n_{\text{pix}}} R_{n,m} \xi_n^2 \eta_m^2 \\
F_{46} &= \frac{A^2}{2} \sum_{n=0, m=0}^{n_{\text{pix}}} R_{n,m} \xi_n^3 \eta_m \\
F_{55} &= \frac{A^2}{4} \sum_{n=0, m=0}^{n_{\text{pix}}} R_{n,m} \eta_m^4 \\
F_{56} &= \frac{A^2}{2} \sum_{n=0, m=0}^{n_{\text{pix}}} R_{n,m} \eta_m^3 \xi_n \\
F_{66} &= A^2 \sum_{n=0, m=0}^{n_{\text{pix}}} R_{n,m} \xi_n^2 \eta_m^2,
\end{aligned} \tag{C.1}$$

where $R_{n,m} = \frac{\delta_x^2 \delta_y^2 E_{n,m}^2}{2\sigma^2}$ and

$E_{n,m} = \exp\left(-\frac{1}{2} (c_1(x_n - x_0)^2 + 2c_3(x_n - x_0)(y_m - y_0) + c_2(y_m - y_0)^2)\right)$. $\xi_n = x_n - x_0$ and $\eta_m = y_m - y_0$.

Appendix D. Derivation of the odd integrals

We start from :

$$J_{x^i y^j} = \int_{a-u_x}^{a+u_x} \int_{-b}^b f_{i,j}(x, y) dx dy + \int_{-a}^a \int_{b-u_y}^{b+u_y} f_{i,j}(x, y) dx dy \tag{D.1}$$

With $f_{i,j}(x, y) = x^i y^j \exp\left(-\frac{1}{2} (c_1 x^2 + 2c_3 xy + c_2 y^2)\right)$. The expression of $J_{x^i y^j}$ is computed by integrating by part to get rid of the polynomial factor and then integrating the univariate Gaussian function using the error function. Finally

we get :

$$J_x = -\frac{u_y b c_3 \pi}{c_1^{3/2}} \exp\left(-\frac{D b^2}{c_1}\right) \left(\operatorname{erf}\left(\frac{a c_1 + b c_3}{\sqrt{c_1}}\right) + \operatorname{erf}\left(\frac{b c_3}{\sqrt{c_1}}\right) \right) + \frac{u_y}{c_1} \exp(-c_1 a^2 - c_2 b^2 - 2 c_3 a b) \quad (\text{D.2})$$

$$J_{x^3} = -2 \frac{u_y b c_3 \pi^{1/2}}{c_1^{5/2}} \left(\frac{3}{4} + \frac{c_3^2 b^2}{2 c_1} \right) \times \exp\left(-\frac{D b^2}{c_1}\right) \left(\operatorname{erf}\left(\frac{a c_1 + b c_3}{\sqrt{c_1}}\right) + \operatorname{erf}\left(\frac{a c_1 - b c_3}{\sqrt{c_1}}\right) \right) + \frac{u_x a^3 \sqrt{\pi}}{c_2^{1/2}} \exp\left(-\frac{D a^2}{c_2}\right) \left(\operatorname{erf}\left(\frac{b c_2 + a c_3}{\sqrt{c_2}}\right) + \operatorname{erf}\left(\frac{b c_2 - a c_3}{\sqrt{c_2}}\right) \right) \quad (\text{D.3})$$

$$J_{x y^2} = -\frac{u_y b^3 c_3 \pi^{1/2}}{c_1^{3/2}} \exp\left(-\frac{D b^2}{c_1}\right) \left(\operatorname{erf}\left(\frac{a c_1 + b c_3}{\sqrt{c_1}}\right) + \operatorname{erf}\left(\frac{a c_1 - b c_3}{\sqrt{c_1}}\right) \right) + \frac{u_x a^3 c_3^2 \pi^{1/2}}{c_2^{5/2}} \exp\left(-\frac{D a^2}{c_2}\right) \left(\operatorname{erf}\left(\frac{b c_2 + a c_3}{\sqrt{c_2}}\right) + \operatorname{erf}\left(\frac{b c_2 - a c_3}{\sqrt{c_2}}\right) \right) + \frac{u_x a \pi^{1/2}}{2 c_2^{3/2}} \exp\left(-\frac{D a^2}{c_2}\right) \left(\operatorname{erf}\left(\frac{b c_2 + a c_3}{\sqrt{c_2}}\right) + \operatorname{erf}\left(\frac{b c_2 - a c_3}{\sqrt{c_2}}\right) \right) \quad (\text{D.4})$$

Equivalent results are obtained for $J_y, J_{y^3}, J_{x^2 y}$.

Appendix E. Illustration computation of $\mathbf{e} J_{x^i y^j}$ (Eq. 9) for even case ($\mathbf{i+j}$ even)

The general strategy is to use firstly to compute $\tilde{M}_{x^i y^j}$ defined in eq. 20, secondly to use $N_{x^i y^j}$ given in Appendix F and then to compute $J_{x^i y^j}$ using 15 and the fact that $\tilde{M}_{x^i y^j} \simeq M_{x^i y^j}$. Since $N_{x^i y^j}$ is already given in [19] most of the work is on computing $\tilde{M}_{x^i y^j}$.

case $\mathbf{i=2, j=0}$ We first compute \tilde{M}_{x^2} . According to Eq. 19 we have :

$$\begin{aligned}\tilde{M}_{x^2} = & 2 \int_{(-\infty; -a] \times R} x^2 \exp(- (c_1 x^2 + 2c_3 xy + c_2 y^2)) dx dy \\ & + 2 \int_{R \times (-\infty; -b]} x^2 \exp(- (c_1 x^2 + 2c_3 xy + c_2 y^2)) dx dy.\end{aligned}\quad (\text{E.1})$$

We integrate along one axis in each integral and get :

$$\begin{aligned}\tilde{M}_{x^2} = & 2 \sqrt{\frac{\pi}{c_2}} \int_{-\infty}^{-a} x^2 \exp\left(-\left(\frac{x^2 D}{c_2}\right)\right) dx \\ & + 2 \frac{c_3^2 \sqrt{\pi}}{c_1^{5/2}} \int_{-\infty}^{-b} y^2 \exp\left(-\left(\frac{y^2 D}{c_1}\right)\right) dy \\ & + \frac{\sqrt{\pi}}{c_1^{3/2}} \int_{-\infty}^{-b} \exp\left(-\left(\frac{y^2 D}{c_1}\right)\right) dy.\end{aligned}\quad (\text{E.2})$$

Each term can be simplified using integration by part:

$$\begin{aligned}2 \sqrt{\frac{\pi}{c_2}} \int_{-\infty}^{-a} x^2 e^{(-\frac{x^2 D}{c_2})} dx &= -\frac{\sqrt{\pi c_2}}{D} \left[x e^{(-\frac{x^2 D}{c_2})} \right]_{-\infty}^{-a} + \frac{c_2}{D} \sqrt{\frac{\pi}{c_2}} \int_{-\infty}^{-a} e^{(-\frac{x^2 D}{c_2})} dx, \\ &= \frac{a \sqrt{\pi c_2}}{D} e^{(-\frac{a^2 D}{c_2})} + \frac{c_2}{D} \sqrt{\frac{\pi}{c_2}} \int_{-\infty}^{-a} e^{(-\frac{x^2 D}{c_2})} dx,\end{aligned}\quad (\text{E.3})$$

and

$$\begin{aligned}& 2 \frac{c_3^2 \sqrt{\pi}}{c_1^{5/2}} \int_{-\infty}^{-b} y^2 \exp\left(-\left(\frac{y^2 D}{c_1}\right)\right) dy \\ &= \frac{c_3^2 b \sqrt{\pi}}{D c_1^{3/2}} \exp\left(\frac{-b^2 D}{c_1}\right) + \frac{\sqrt{\pi} c_3^2}{D c_1^{3/2}} \int_{-\infty}^{-b} \exp\left(-\frac{y^2 D}{c_1}\right) dy.\end{aligned}\quad (\text{E.4})$$

So finally summing everything leads to:

$$\begin{aligned}\tilde{M}_{x^2} = & \frac{a \sqrt{\pi c_2}}{D} e^{(-\frac{a^2 D}{c_2})} + \frac{c_2}{D} \sqrt{\frac{\pi}{c_2}} \int_{-\infty}^{-a} e^{(-\frac{x^2 D}{c_2})} dx \\ & + \frac{c_3^2 b \sqrt{\pi}}{D c_1^{3/2}} e^{(-\frac{b^2 D}{c_1})} + \left(\frac{\sqrt{\pi} c_3^2}{D c_1^{3/2}} + \frac{\sqrt{\pi}}{c_2^{3/2}} \right) \int_{-\infty}^{-b} e^{(-\frac{y^2 D}{c_1})} dy.\end{aligned}\quad (\text{E.5})$$

Using a integration by part and under the assumption that a and b are large relative to $\sqrt{\frac{c_2}{D}}$ and $\sqrt{\frac{c_1}{D}}$ leads to:

$$\int_{-\infty}^{-a} \exp\left(-x^2 \frac{D}{c_2}\right) \simeq \frac{c_2}{2Da} \exp\left(\frac{-a^2 D}{c_2}\right),\quad (\text{E.6})$$

This can be used to simplify E.5:

$$\begin{aligned}\tilde{M}_{x^2} &= \frac{a\sqrt{\pi c_2}}{D} \exp\left(-\frac{a^2 D}{c_2}\right) + \frac{c_2^{3/2}}{2aD^2} \sqrt{\pi} \exp\left(-\frac{a^2 D}{c_2}\right) \\ &\quad + \frac{c_3^2 b \sqrt{\pi}}{D c_1^{3/2}} \exp\left(\frac{-b^2 D}{c_1}\right) \\ &\quad + \left(\frac{\sqrt{\pi} c_3^2}{D c_1^{3/2}} + \frac{\sqrt{\pi}}{c_2^{3/2}}\right) \frac{c_1}{2Db} \exp\left(-\frac{b^2 D}{c_1}\right).\end{aligned}\quad (\text{E.7})$$

Reordering the terms:

$$\begin{aligned}\tilde{M}_{x^2} &= \exp\left(-\frac{a^2 D}{c_2}\right) \left(\frac{a\sqrt{\pi c_2}}{D} + \frac{c_2^{3/2}}{2aD^2} \sqrt{\pi}\right) \\ &\quad + \exp\left(-\frac{b^2 D}{c_1}\right) \left(\frac{c_3^2 b \sqrt{\pi}}{D c_1^{3/2}} + \left(\frac{\sqrt{\pi} c_3^2}{D c_1^{3/2}} + \frac{\sqrt{\pi}}{c_2^{3/2}}\right) \frac{c_1}{2Db}\right).\end{aligned}\quad (\text{E.8})$$

Finally the truncated signal is (assuming $\tilde{M}_{x^2} = M_{x^2}$)

$$J_{x^2} = N_{x^2} - \tilde{M}_{x^2}, \quad (\text{E.9})$$

so we get :

$$\begin{aligned}J_{x^2} &= \frac{\pi c_2}{2D^{3/2}} - \exp\left(-\frac{a^2 D}{c_2}\right) \left(\frac{a\sqrt{\pi c_2}}{D} + \frac{c_2^{3/2}}{2aD^2} \sqrt{\pi}\right) \\ &\quad - \exp\left(-\frac{b^2 D}{c_1}\right) \left(\frac{c_3^2 b \sqrt{\pi}}{D c_1^{3/2}} + \left(\frac{\sqrt{\pi} c_3^2}{D c_1^{3/2}} + \frac{\sqrt{\pi}}{c_2^{3/2}}\right) \frac{c_1}{2Db}\right).\end{aligned}\quad (\text{E.10})$$

By exchanging the role of x and y in the previous derivation, an expression for J_{y^2} is:

$$\begin{aligned}J_{y^2} &= \frac{\pi c_1}{2D^{3/2}} - \exp\left(-\frac{b^2 D}{c_1}\right) \left(\frac{b\sqrt{\pi c_1}}{D} + \frac{c_1^{3/2}}{2bD^2} \sqrt{\pi}\right) \\ &\quad - \exp\left(-\frac{a^2 D}{c_2}\right) \left(\frac{c_3^2 a \sqrt{\pi}}{D c_2^{3/2}} + \left(\frac{\sqrt{\pi} c_3^2}{D c_2^{3/2}} + \frac{\sqrt{\pi}}{c_1^{3/2}}\right) \frac{c_2}{2Da}\right).\end{aligned}\quad (\text{E.11})$$

case $i=0, j=0$

The calculations are very similar for \tilde{M} . \tilde{M} is defined as:

$$\begin{aligned}\tilde{M} &= 2 \int_{(-\infty, -a] \times R} \exp\left(-\left(c_1 x^2 + 2c_3 xy + c_2 y^2\right)\right) dx dy \\ &\quad + 2 \int_{R \times (-\infty, -b]} \exp\left(-\left(c_1 x^2 + 2c_3 xy + c_2 y^2\right)\right) dx dy\end{aligned}\quad (\text{E.12})$$

And when integrating over y for for the first integral and x for the second one gets:

$$\begin{aligned}\tilde{M} = & 2\sqrt{\frac{\pi}{c_2}} \int_{[-\infty; -a]} \exp\left(-\left(\frac{D}{c_2}x^2\right)\right) dx dy \\ & + 2\sqrt{\frac{\pi}{c_1}} \int_{(-\infty; -b]} \exp\left(-\left(\frac{D}{c_1}y^2\right)\right) dx dy\end{aligned}\quad (\text{E.13})$$

Using the approximation in (E.6) we get:

$$\tilde{M} = \frac{\sqrt{\pi c_2}}{Da} \exp\left(-\frac{D}{c_2}a^2\right) + \frac{\sqrt{\pi c_1}}{Db} \exp\left(-\frac{D}{c_1}b^2\right)\quad (\text{E.14})$$

Case $i=1$ $j=1$

The same technique is used to compute the surplus $\tilde{M}_{x,y}$ defined in Eq. 16. In the first step:

$$\begin{aligned}\int_{-\infty}^{-a} \int_{-\infty}^{\infty} xy \exp(-c_1x^2 - c_2y^2 - 2c_3xy) dx dy \\ = -\frac{\sqrt{\pi}c_3}{2D\sqrt{c_2}} \exp\left(-\frac{Da^2}{c_2}\right) \left(a + \frac{c_2}{2\sqrt{Da}}\right).\end{aligned}\quad (\text{E.15})$$

By exchanging the role of x and y in the previous equation we get:

$$\begin{aligned}\int_{-\infty}^{-\infty} \int_{-\infty}^{-b} xy \exp(-c_1x^2 - c_2y^2 - 2c_3xy) dx dy \\ = -\frac{\sqrt{\pi}c_3}{2D\sqrt{c_1}} \exp\left(-\frac{Db^2}{c_1}\right) \left(b + \frac{c_1}{2\sqrt{Db}}\right).\end{aligned}$$

So the surplus is approximately:

$$\begin{aligned}\tilde{M}_{xy} = & -\frac{\sqrt{\pi}c_3}{D\sqrt{c_1}} \exp\left(-\frac{Db^2}{c_1}\right) \left(b + \frac{c_1}{2\sqrt{Db}}\right) \\ & - \frac{\sqrt{\pi}c_3}{D\sqrt{c_2}} \exp\left(-\frac{Da^2}{c_2}\right) \left(a + \frac{c_2}{2\sqrt{Da}}\right)\end{aligned}\quad (\text{E.16})$$

Using Eq. 15, we obtain the following expression :

$$\begin{aligned}J_{xy} = & N_{xy} + \frac{\sqrt{\pi}c_3}{D\sqrt{c_1}} \exp\left(-\frac{Db^2}{c_1}\right) \left(b + \frac{c_1}{2\sqrt{Db}}\right) \\ & + \frac{\sqrt{\pi}c_3}{D\sqrt{c_2}} \exp\left(-\frac{Da^2}{c_2}\right) \left(a + \frac{c_2}{2\sqrt{Da}}\right) \\ = & -\frac{c_3\pi}{2D^{3/2}} + \frac{\sqrt{\pi}c_3}{D\sqrt{c_1}} \exp\left(-\frac{Db^2}{c_1}\right) \left(b + \frac{c_1}{2\sqrt{Db}}\right) \\ & + \frac{\sqrt{\pi}c_3}{D\sqrt{c_2}} \exp\left(-\frac{Da^2}{c_2}\right) \left(a + \frac{c_2}{2\sqrt{Da}}\right).\end{aligned}\quad (\text{E.17})$$

where N_{xy} is given in Appendix F.

Unfortunately, those expressions remain complex so it can be advantageous to keep the dominant terms and get :

$$J_{x^2} = N_{x^2} - \frac{a\sqrt{\pi c_2}}{D} \exp\left(-\frac{a^2 D}{c_2}\right) - \frac{c_3^2 b \sqrt{\pi}}{D c_1^{3/2}} \exp\left(-\frac{b^2 D}{c_1}\right) \quad (\text{E.18})$$

$$J_{y^2} = N_{y^2} - \frac{b\sqrt{\pi c_1}}{D} \exp\left(-\frac{b^2 D}{c_1}\right) - \frac{c_3^2 a \sqrt{\pi}}{D c_2^{3/2}} \exp\left(-\frac{a^2 D}{c_2}\right) \quad (\text{E.19})$$

$$J_{xy} = N_{xy} + \frac{\sqrt{\pi} b c_3}{D \sqrt{c_1}} \exp\left(-\frac{D b^2}{c_1}\right) + \frac{\sqrt{\pi} a c_3}{D \sqrt{c_2}} \exp\left(-\frac{D a^2}{c_2}\right) \quad (\text{E.20})$$

The computation of J_{x^2} , J_{y^2} , J_{xy} is sufficient to compute $F_{2,2}$, $F_{2,3}$ and $F_{3,3}$.

Case i=2 j=2

We follow the same procedure as in the previous paragraph by computing. We have: $\tilde{M}_{x^2 y^2}$:

$$\begin{aligned} & \int_{-\infty}^{-a} \int_{-\infty}^{\infty} x^2 y^2 \exp(-c_1 x^2 - c_2 y^2 - 2c_3 xy) dx dy \\ &= \frac{2\pi c_3^2 + \pi c_2 c_1}{8D^{3/2}} \left(1 - \operatorname{erf}\left(\frac{a\sqrt{D}}{\sqrt{c_2}}\right)\right) \\ & \quad + \frac{\sqrt{\pi} c_3^2 a^3}{2D c_2^{3/2}} \exp\left(-\frac{a^2 D}{c_2}\right) + \frac{2aD^{1/2}}{\sqrt{\pi c_2}} \pi \frac{2c_3 + c_1 c_2}{4D^{5/2}} \end{aligned} \quad (\text{E.21})$$

and also:

$$\begin{aligned} & \int_{-\infty}^{-a} \int_{-\infty}^{\infty} x^2 y^2 \exp(-c_1 x^2 - c_2 y^2 - 2c_3 xy) dx dy \\ &= \frac{2\pi c_3^2 + \pi c_2 c_1}{8D^{3/2}} \left(1 - \operatorname{erf}\left(\frac{b\sqrt{D}}{\sqrt{c_1}}\right)\right) + \frac{\sqrt{\pi} c_3^2 b^3}{2D c_1^{3/2}} \exp\left(-\frac{b^2 D}{c_1}\right) \\ & \quad + \frac{2bD^{1/2}}{\sqrt{\pi c_1}} \pi \frac{2c_3 + c_1 c_2}{4D^{5/2}} \exp\left(-\frac{b^2 D}{c_1}\right). \end{aligned} \quad (\text{E.22})$$

So the surplus becomes:

$$\begin{aligned}
\tilde{M}_{x^2y^2} &= \frac{2\pi c_3^2 + \pi c_2 c_1}{4D^{3/2}} \left(2 - \operatorname{erf} \left(\frac{a\sqrt{D}}{\sqrt{c_2}} \right) - \operatorname{erf} \left(\frac{b\sqrt{D}}{\sqrt{c_1}} \right) \right) \\
&+ \frac{\sqrt{\pi} c_3^2 b^3}{D c_1^{3/2}} \exp \left(-\frac{b^2 D}{c_1} \right) + \frac{4bD^{1/2}}{\sqrt{\pi} c_1} \pi \frac{2c_3 + c_1 c_2}{4D^{5/2}} \exp \left(-\frac{b^2 D}{c_1} \right) \\
&+ \frac{\sqrt{\pi} c_3^2 a^3}{D c_2^{3/2}} \exp \left(-\frac{a^2 D}{c_2} \right) + \frac{4aD^{1/2}}{\sqrt{\pi} c_2} \pi \frac{2c_3 + c_1 c_2}{4D^{5/2}}
\end{aligned} \tag{E.23}$$

where we used the approximation:

$$1 - \operatorname{erf} \left(a \frac{\sqrt{D}}{\sqrt{c_2}} \right) \simeq \frac{\sqrt{c_2}}{\sqrt{\pi} D a} \exp \left(-a^2 \frac{D}{c_2} \right). \tag{E.24}$$

To obtain a compact form for \tilde{M}_{x^2,y^2} we can plug in $N_{x^2y^2}$ from Appendix F in Eq. E.23 and get:

$$\begin{aligned}
\tilde{M}_{x^2y^2} &= \frac{DN_{x^2y^2}}{3\sqrt{\pi}} \left(\frac{\sqrt{c_2}}{a\sqrt{D}} \exp \left(-\frac{a^2 D}{c_2} \right) + \frac{\sqrt{c_1}}{b\sqrt{D}} \exp \left(-\frac{b^2 D}{c_1} \right) \right) \\
&+ \frac{4}{3\sqrt{\pi}} N_{x^2y^2} \left(\frac{aD^{1/2}}{\sqrt{c_2}} \exp \left(-\frac{a^2 D}{c_2} \right) + \frac{bD^{1/2}}{\sqrt{c_1}} \exp \left(-\frac{b^2 D}{c_1} \right) \right) \\
&+ \frac{\sqrt{\pi} c_3^2 b^3}{D c_2^{3/2}} \exp \left(-\frac{b^2 D}{c_1} \right) + \frac{\sqrt{\pi} c_3^2 a^3}{D} \exp \left(-\frac{a^2 D}{c_2} \right)
\end{aligned} \tag{E.25}$$

case i=4 j=0

We follow the same procedure as in the previous paragraph by computing \tilde{M}_{x^4} .

We have :

$$\begin{aligned}
&\int_{-\infty}^{-a} \int_{-\infty}^{-\infty} x^4 \exp(-c_1 x^2 - c_2 y^2 - 2c_3 xy) dx dy = \frac{3c_2^2 \sqrt{\pi} c_2}{8D^3 a} \exp \left(-a^2 \frac{D}{c_2} \right) \\
&- \frac{\sqrt{\pi} a^3 c_3^2 \sqrt{c_2}}{2D^2} \exp \left(-\frac{a^2 D}{c_2} \right) + \frac{3c_2^{3/2} a \sqrt{\pi}}{4D^2} \exp \left(-\frac{a^2 D}{c_2} \right) + \frac{a^3 c_1 c_2^{3/2} \sqrt{\pi}}{2D^2} \exp \left(-\frac{a^2 D}{c_2} \right)
\end{aligned}$$

and

$$\begin{aligned}
&\int_{-\infty}^{\infty} \int_{-\infty}^{-b} x^4 \exp(-c_1 x^2 - c_2 y^2 - 2c_3 xy) dx dy = \frac{c_3 b^3 \pi^{1/2}}{c_1^{1/2} D^{1/2}} \exp \left(-\frac{Db^2}{c_1} \right) \\
&- \frac{3c_3 b \sqrt{c_1} \pi}{4D^2} \exp \left(-\frac{Db^2}{c_1} \right) + \frac{3}{4} \frac{\sqrt{\pi} c_1^{3/2} c_3}{bD^3} \exp \left(-\frac{Db^2}{c_1} \right)
\end{aligned} \tag{E.26}$$

So the surplus becomes:

$$\begin{aligned} \tilde{M}_{x^4} = & 2 \left(\frac{1}{2} \frac{\sqrt{\pi} b^3 c_3^4}{c_1^{7/2} D} + \frac{3c_2^2 c_2 b \sqrt{\pi}}{2c_1^{3/2} D^2} - \frac{3b\pi^{1/2} c_3^4}{4c_1^{5/2} D^2} - \frac{3\sqrt{\pi} c_1 c_2^2}{4D^3 b} \right) \exp\left(-\frac{b^2 D}{c_1}\right) \\ & + 2 \left(\frac{3c_2^2 \sqrt{\pi} c_2}{8D^3 a} + \frac{3c_2^{3/2} a \sqrt{\pi}}{4D^2} + \frac{a^3 c_2^{1/2} \sqrt{\pi}}{2D} \right) \exp\left(-\frac{a^2 D}{c_2}\right) \end{aligned} \quad (\text{E.27})$$

J_{x^4} is then computed using equation 15 and the expression for N_{x^4} given in Appendix F.

Appendix F. Expressions for the $N_{x,y}$

The expressions for N_{x^i, y^j} are classical and already derived in [19]. They are recalled here for completeness

$$N_x = 0. \quad (\text{F.1})$$

$$N_{x^3} = 0 \quad (\text{F.2})$$

$$N_{y^3} = 0 \quad (\text{F.3})$$

$$N_{xy^2} = 0 \quad (\text{F.4})$$

$$N_{x^2 y} = 0 \quad (\text{F.5})$$

$$N_{x^3 y} = 0 \quad (\text{F.6})$$

$$N_{y^3 x} = 0 \quad (\text{F.7})$$

$$N = \frac{\pi}{\sqrt{D}}, \quad (\text{F.8})$$

$$N_{x^2} = \frac{1}{2} \frac{\pi c_2}{D^{3/2}}, \quad (\text{F.9})$$

$$N_{y^2} = \frac{1}{2} \frac{\pi c_1}{D^{3/2}}, \quad (\text{F.10})$$

$$N_{y^4} = \frac{3}{4} \frac{c_1^2 \pi}{D^{5/2}}, \quad (\text{F.11})$$

$$N_{x^4} = \frac{3}{4} \frac{c_2^2 \pi}{D^{5/2}}, \quad (\text{F.12})$$

$$N_{xy} = -\frac{1}{2} \frac{c_3 \pi}{D^{3/2}}, \quad (\text{F.13})$$

$$N_{x^2 y^2} = \frac{3}{4} \frac{\pi (c_1 c_2 + 2 c_3^2)}{D^{5/2}}. \quad (\text{F.14})$$

Appendix G. The centroid

The centroid method is a classical alternative to estimate the signal centroid. This does not make any assumption with regards to the signal shape. It is defined as

$$x_0 = \frac{\sum_{n,m} x_n E_{n,m}}{\sum_{n,m} E_{n,m}} \quad (\text{G.1})$$

$$y_0 = \frac{\sum_{n,m} y_m E_{n,m}}{\sum_{n,m} E_{n,m}} \quad (\text{G.2})$$